

1 **Illuminating the pre-, co-, and post-seismic phases of**
2 **the 2016 M7.8 Kaikōura earthquake with 10 years of**
3 **seismicity**

4 **C. J. Chamberlain¹, W. B. Frank², F. Lanza³, J. Townend¹, E. Warren-Smith⁴**

5 ¹School of Geography, Environment and Earth Sciences, Victoria University of Wellington, Wellington,
6 New Zealand

7 ²Department of Earth, Atmospheric and Planetary Sciences, Massachusetts Institute of Technology,
8 Cambridge, MA, USA

9 ³Swiss Seismological Service, ETH Zürich, Switzerland

10 ⁴GNS Science, Lower Hutt, New Zealand

11 **Key Points:**

- 12 • 10-year long matched-filter derived catalog of 33,242 earthquakes surrounding the
13 2016 Kaikōura earthquake.
14 • Observed offshore reverse faulting provides a direct and viable rupture pathway.
15 • No detectable seismicity occurs on the subduction interface, and any deformation
16 there is aseismic.

Corresponding author: Calum J. Chamberlain, calum.chamberlain@vuw.ac.nz

Abstract

The 2016 M7.8 Kaikōura earthquake is one of the most complex earthquakes in recorded history, with significant rupture of at least 21 crustal faults. Using a matched-filter detection routine, precise cross-correlation pick corrections, and accurate location and re-location techniques, we construct a catalog of 33,242 earthquakes between 2009 and 2019 on and adjacent to the faults that ruptured in the Kaikōura earthquake. We also compute focal mechanisms for 1,755 of the earthquakes used as templates. Using this catalog we reassess the rupture pathway of the Kaikōura earthquake. In particular we show that: (1) the earthquake nucleated on the Humps Fault; (2) there is a likely linking offshore reverse fault between the southern fault system and the Papatea Fault, which can explain the anomalously high slip on the Papatea Fault; (3) the faults that ruptured in the 2013 Cook Strait sequence were reactivated by the Kaikōura earthquake and may have played a role in the termination of the earthquake; and (4) no seismicity on an underlying subduction interface is observed beneath almost all of the ruptured region suggesting that if deformation did occur on the plate interface then it occurred aseismically and did not play a significant role in generating co-seismic ground motion.

Plain Language Summary

The 2016 Kaikōura earthquake in the South Island of New Zealand, is one of the most complex earthquakes reported. While extensive geological work has been undertaken to map the surface faulting in the earthquake, it remains unclear how these faults are linked together at depth. In this paper we document the construction of a dense, long-duration catalog of earthquakes that occurred on and around the faults that slipped in the Kaikōura earthquake. Using this catalog of 33,242 earthquakes we are able to illuminate likely sub-surface links between faults and investigate how these faults slipped before and after the Kaikōura earthquake. We show that offshore faults provide a link between the southern faults, where the earthquake started, and the northern faults, where the highest slip occurred. We also show that the earthquake stopped on faults that had previously slipped in the 2013 Cook Strait earthquakes, and which likely played a role in earthquake arrest. Finally we see no evidence for elevated seismicity on the underlying subduction interface beneath the faults that slipped in the Kaikōura earthquake.

1 Introduction

The November 2016 Kaikōura M 7.8 earthquake ruptured at least 21 faults in the Marlborough Fault Zone at the transition from subduction on the Hikurangi subduction zone to on-land transpression (Figure 1; Kaiser et al., 2017; Hamling et al., 2017; Litchfield et al., 2018). This complex earthquake involved a wide range of co-seismic faulting styles, producing dextral, sinistral, reverse and normal surface ruptures (Clark et al., 2017). In addition to the extensive crustal faulting, the underlying subduction interface may have slipped co-seismically (Bai et al., 2017; T. Wang et al., 2018), although regional data show little evidence for this (Hamling et al., 2017; Holden et al., 2017).

The transpressional rupture cascade resulted in significant surface rupture of multiple previously known and unknown faults (Litchfield et al., 2018). The complexity of the earthquake rupture (Hamling et al., 2017) has to date precluded the robust constraint of the role of individual faults within the rupture sequence (e.g. Holden et al., 2017) and the dynamics of the rupture propagation and termination (Ando & Kaneko, 2018; Ulrich et al., 2019). When modelling such complex ruptures, the identification of all major participating faults has a significant impact on where the inferred slip is concentrated (e.g. Hamling et al., 2017) and the propagation sequence from one fault to the next, exemplified by the different rupture pathways modelled by Ando and Kaneko (2018) and Ulrich et al. (2019). The implications of these models are wide ranging: from a general

66 understanding of how earthquakes are able to propagate through complex fault systems,
67 to more local implications for seismic hazard in central New Zealand.

68 Almost all published models of co-seismic and post-seismic deformation in the Kaikōura
69 earthquake have been based on simplified fault models derived from near-surface geo-
70 logical data (e.g. Hamling et al., 2017; Xu et al., 2018; T. Wang et al., 2018; Holden et
71 al., 2017; Clark et al., 2017). While these data provide essential controls, they do not
72 provide robust information on the fault structure at depth, where most of the slip hap-
73 pens during earthquakes. Accurate earthquake catalogs provide a viable tool to constrain
74 fault geometry at depth (e.g. Plesch et al., 2020), but have thus far been unavailable for
75 the Kaikōura region, apart from the relatively small catalog developed by Lanza et al.
76 (2019), and sparse moment tensor analysis by Cesca et al. (2017). Such catalogs of seis-
77 micity can also help illuminate other elements of the Kaikōura earthquake, including its
78 relationship to prior seismicity in New Zealand, and how the various faults respond post-
79 seismically.

80 1.1 Co-seismic kinematics and rupture propagation

81 Kinematic rupture models (Holden et al., 2017) show that the Kaikōura rupture
82 started slowly on the Humps–Hundalee Fault system (Nicol et al., 2018; J. N. Williams
83 et al., 2018). However, hypocentre estimates of the Kaikōura earthquake vary from be-
84 ing consistent with nucleation on the Humps Fault (Lanza et al., 2019; Nicol et al., 2018),
85 to being as much as 7–15 km off the Humps Fault (according to the GeoNet¹ and USGS
86 solutions respectively²).

87 Once initiated, the rupture propagated north-west towards the Hope Fault, but only
88 produced a minor surface rupture (Hamling et al., 2017; Litchfield et al., 2018) of this
89 fault, which previous paleoseismic studies have indicated to have a high Quaternary slip-
90 rate (Litchfield et al., 2018). The rupture then stepped onto the Jordan Thrust–Kekerengu
91 system where the maximum co-seismic surface offset of 11.8 m dextral occurred on the
92 Kekerengu Fault (Kearse et al., 2018). The dominantly N–S-striking Papatea Fault, which
93 intersects the junction between the Jordan Thrust and the Kekerengu Fault, also rup-
94 tured with up to 9.5 m of uplift and 6.1 m of sinistral motion (R. M. Langridge et al.,
95 2018). Previous authors (e.g. Hamling et al., 2017; Holden et al., 2017) have noted that
96 the high slip on the short (c. 19 km long) Papatea fault cannot be fit by elastic rupture
97 models. The Papatea Fault intersects the Jordan Thrust–Kekerengu system at the point
98 where dextral slip increases from the Jordan Thrust to the Kekerengu, and on-fault dip-
99 slip motion changes sense, from normal on the Jordan Thrust to reverse on the Kekerengu
100 (Kearse et al., 2018). This normal motion (NW down) on the Jordan Thrust appears
101 not to be the dominant long-term sense of motion, with higher mountains on the NW
102 side attesting to the dominantly oblique-reverse motion on the Jordan Thrust and Up-
103 per Kowhai Faults on geological timescales (Van Dissen & Yeats, 1991).

104 The details of the rupture pathway between the southern Humps–Hundalee fault
105 system and the Kekerengu Fault are not well-resolved and two main pathways have been
106 postulated. Firstly, the offshore route, from the Hundalee Fault to the Papatea Fault via
107 mostly unmapped offshore thrust faults. This trajectory appears consistent with a range
108 of observations including off-fault damage at the Papatea–Jordan Thrust–Kekerengu junc-
109 tion (Klinger et al., 2018), kinematic (Holden et al., 2017) and dynamic rupture simu-
110 lations (Ulrich et al., 2019), and tsunami modelling (Gusman et al., 2018; Bai et al., 2017).
111 The second scenario involves rupture jumping from the Hundalee Fault to the Upper Kowhai
112 Fault and onto the Jordan Thrust and Kekerengu Faults with limited slip on the inter-
113 mediate Whites (Ando & Kaneko, 2018) and inferred Snowflake Spur Faults (Zinke et

¹ <https://www.geonet.org.nz/earthquake/technical/2016p858000> last accessed 24 April 2021

² <https://earthquake.usgs.gov/earthquakes/eventpage/us1000778i> last accessed 24 April 2021

114 al., 2019). The lack of resolution of the fault network and possible inter-connections at
 115 depth inferred from surface observations alone mean that it remains unclear which sce-
 116 nario actually occurred.

117 The rupture continued to propagate northwards onto the Needles Fault and other
 118 faults in the Cape Campbell region before terminating near Cape Campbell itself (Kearse
 119 et al., 2018), in the region of the 2013 M_W 6.6 Cook Strait and Lake Grassmere earth-
 120 quakes (Hamling et al., 2014). This northward rupture propagation resulted in strong
 121 shaking in New Zealand’s capital city, Wellington (Kaiser et al., 2017; Bradley et al., 2017).
 122 The reasons for rupture terminating near Cape Campbell, despite the availability of faults
 123 straddling Cook Strait (Kearse et al., 2018), remains unclear. Dynamic rupture mod-
 124 els (Ando & Kaneko, 2018; Ulrich et al., 2019) are able to capture most of the major fea-
 125 tures of the Kaikōura rupture, including the absence of slip on the Hope Fault, maxi-
 126 mum co-seismic offset, and the termination near Cape Campbell. However, how these
 127 two models achieve termination at Cape Campbell differs: Ando and Kaneko (2018) ac-
 128 count for the termination by a c. 10° rotation in the prevailing stress field, which is in-
 129 dicated by focal mechanism inversions (Balfour et al., 2005; Townsend et al., 2012). In
 130 contrast Ulrich et al. (2019) do not invoke a stress rotation, and instead artificially re-
 131 duce the stress on the Needles Fault. Neither modelling study includes the more favourably-
 132 oriented faults that ruptured in the 2013 Cook Strait sequence.

133 In addition to the upper crustal faulting complexities, it remains unclear what role
 134 the underlying subduction interface played in the Kaikōura earthquake (Hamling, 2020).
 135 Lamb et al. (2018) suggested that the pattern of strain accumulation on the interface
 136 can explain the diversity of crustal faulting, but it is not clear that the interface played
 137 an active co-seismic role. Different models and data suggest differing contributions from
 138 the subduction interface to the co-seismic moment budget of the Kaikōura earthquake.
 139 Generally, models derived from regional data (e.g. Hamling et al., 2017; Gusman et al.,
 140 2018; Holden et al., 2017) require negligible seismic moment on the underlying interface.
 141 In contrast, studies using teleseismic data tend to favour more slip occurring on the sub-
 142 duction interface (e.g. T. Wang et al., 2018; Bai et al., 2017). Whether the subduction
 143 interface beneath the northern South Island can slip seismically is fundamentally impor-
 144 tant to understanding seismic hazard in this populous region of New Zealand (Wallace
 145 et al., 2018).

146 **1.2 Post-seismic Response**

147 Afterslip inferred using geodetic data from the Kaikōura fault system for the months
 148 following the earthquake shows significant afterslip on the faults known to have ruptured
 149 (Wallace et al., 2018; Mouslopoulou et al., 2019) accompanied by afterslip or triggered
 150 slow-slip on the underlying subduction interface (Wallace et al., 2017; Yu et al., 2020;
 151 Mouslopoulou et al., 2019) and triggered slow-slip in other regions of the Hikurangi mar-
 152 gin (Wallace et al., 2017). However, these models have used a relatively simple model
 153 of crustal faulting that does not capture the spatial extent of aftershocks, in part due
 154 to a lack of a dense, high-precision aftershock catalog.

155 Romanet and Ide (2019) observed tremor occurring prior to the Kaikōura earth-
 156 quake, near the zone of mapped subduction interface afterslip, and suggested that the
 157 tremor may be related to interface slip. However, it is also possible that the tremor lo-
 158 cates on the downdip extent of faults in the Marlborough Fault Zone. Further work is
 159 underway to better constrain these observations. Few aftershocks have yet been reliably
 160 linked to slip on the subduction interface (Lanza et al., 2019).

161 The Kaikōura earthquake generated a significant and ongoing aftershock sequence
 162 (Kaiser et al., 2017) and triggered earthquakes throughout New Zealand (Peng et al.,
 163 2018; Yao et al., 2021). However, it was relatively unproductive compared to average statis-
 164 tics for its magnitude (Chamberlain et al., 2020; Christophersen et al., 2017) resulting

165 in an over-estimation of aftershock rates early in the sequence when average aftershock
 166 behaviour was used in forecasting³. This raises the question of whether complex earth-
 167 quakes have distinct aftershock and afterslip characteristics compared to geometrically
 168 simpler earthquakes.

169 1.3 Unresolved Questions

170 Most models of co- and post-seismic slip around the Kaikōura earthquake have used
 171 multi-fault models of fault ruptures, but these models have generally restricted the avail-
 172 able faults to those with significant surface rupture, or simplifications thereof. The only
 173 study that we are aware of that used aftershocks to better define the rupture geometry
 174 focused on a small number of moment tensor solutions fixed at epicentres computed by
 175 GeoNet (Cesca et al., 2017). We demonstrate in this paper that these GeoNet locations
 176 are poorly constrained due to the use of the IASP91 (Kennett & Engdahl, 1991) 1D ve-
 177 locity model (as also found by Yao et al., 2021; Lanza et al., 2019), rendering them too
 178 inaccurate for use in defining fault structures.

179 Previous analysis of Kaikōura aftershocks (Lanza et al., 2019) has demonstrated
 180 the diffuse nature of aftershocks around the step-over and Cape Campbell regions, which
 181 suggests slip occurred on additional crustal faults. In this paper we expand on this af-
 182 tershock catalog to explore the diversity of faulting around the faults that ruptured in
 183 the Kaikōura earthquake, with the goal of shedding light on the pre-, co- and post-seismic
 184 faulting processes. We particularly focus on several fundamental aspects of the rupture
 185 that remain unresolved:

- 186 1. Rupture Initiation (Section 4.1): Where and how did the Kaikōura earthquake nu-
 187 cleate and were there observable precursory signals?
- 188 2. Rupture Pathway (Section 4.2): What was the likely rupture pathway between
 189 the southern fault system and the high-slip Kekerengu fault and how was this step-
 190 over accommodated kinematically?
- 191 3. Subduction Interface (Section 4.3): What was the seismogenic role of the subduc-
 192 tion interface beneath the known crustal fault ruptures of the Kaikōura earthquake?
- 193 4. Termination (Section 4.4): Why did the rupture terminate at Cape Campbell and
 194 what was the significance of the previous 2013 M_W 6.6 Cook Strait and Lake Grass-
 195 mere earthquakes on this termination?
- 196 5. Post-seismic (Section 4.5): How did such co-seismic complexity affect post-seismic
 197 afterslip?

198 2 Data and Methods

199 To obtain a more detailed picture of the fault geometry at depth, and the pre- and
 200 post-seismic evolution of fault slip, we conducted a matched-filter search to generate a
 201 more complete representation of the seismicity. We analysed >10 years of continuous data
 202 using earthquakes that occurred on the faults that ruptured co- and post-seismically in
 203 the Kaikōura earthquake as template events.

204 We used the catalog of 2,654 aftershocks and the mainshock picked and located by
 205 Lanza et al. (2019) as template events to provide a methodologically consistent set of
 206 phase-picks. This catalog includes every event of $M_L \geq 3$ cataloged by GeoNet that
 207 occurred between 13 November 2016 and 13 May 2017 (UTC) in a rectangular region
 208 between latitudes -43.00° and -40.80° and longitudes 172.75° and 175.20° , apart from 110
 209 earthquakes that had poorly constrained depths. We previously attempted to use the

³ <https://www.geonet.org.nz/earthquake/forecast/kaikoura>, last accessed 22/01/2021

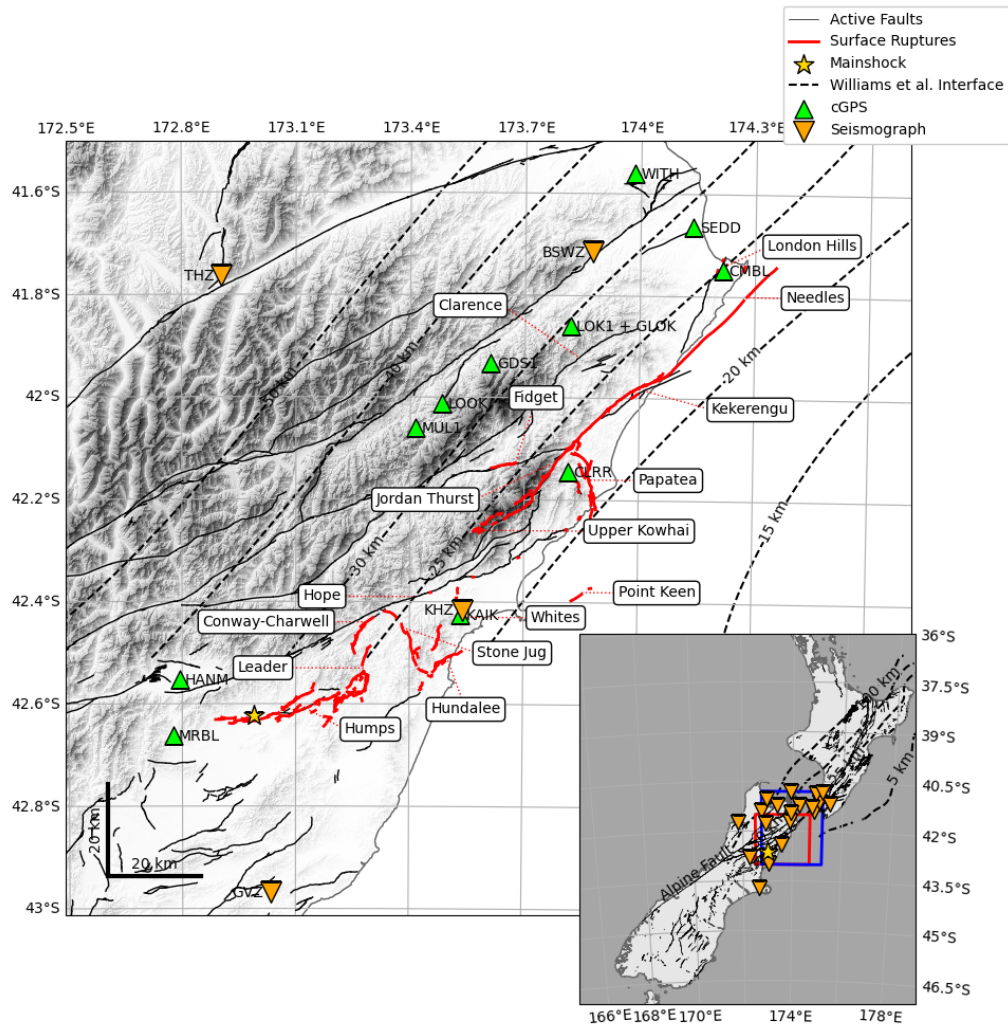


Figure 1. Main panel: GeoNet short-period and broadband seismographs (orange inverted triangles) used in this study and continuous GNSS receivers (green triangles) active during the Kaikōura post-seismic period. Dashed lines mark the modelled subduction interface from C. A. Williams et al. (2013), and solid black lines mark faults of the NZ Active Fault Database (R. Langridge et al., 2016). Red lines mark the mapped surface ruptures of the Kaikōura earthquake (Clark et al., 2017), with names labelled. Inset: Regional setting of the Kaikōura region showing additional seismographs used for detection and location as inverted orange triangles. The location of the main panel is outlined as a red box, the region studied by Lanza et al. (2019) is shown as a blue box and solid and dashed lines are the active fault database and modelled subduction interface respectively.

210 GeoNet catalog directly to construct templates but found that the phase pick-quality
 211 was too variable, and the paucity of S-picks hindered our detection capability: the re-
 212 sulting catalog contained excessive false detections. The Lanza et al. (2019) catalog con-
 213 tains the dominant, moderate-to-large magnitude seismicity recorded in the seven months
 214 following the Kaikōura mainshock.

215 We constructed templates using data from 19 GeoNet broadband and short-period
 216 seismographs (Figure 1). We excluded strong-motion instruments from our analysis due
 217 to their variable timing quality (S. Bannister pers. comm.). Note that these stations were
 218 included in the analysis of Lanza et al. (2019) and may have degraded location quality
 219 in this prior work. We did not include temporary stations (e.g. from the STREWN net-
 220 work, as analysed by Lanza et al. (2019)) in our analysis to exclude bias in detections
 221 arising from variations in network geometry and station density.

222 Templates were made using EQcorrscan (Chamberlain et al., 2018). Continuous
 223 day-long data were detrended, resampled in the frequency-domain to 30.0 Hz to reduce
 224 computational load, filtered using a 4th-order Butterworth bandpass filter between 1.5
 225 and 12 Hz, and trimmed to 4 s length around the P and S phase-picks on the vertical and
 226 horizontal channels respectively. We tested a range of filters and template lengths and
 227 found that using a higher low-cut frequency resulted in additional false detections likely
 228 related to correlations with high-frequency noise, whereas using a lower low-cut frequency
 229 resulted in a degradation of correlations with true detections and an increase in back-
 230 ground (e.g. noise) correlation sums. Increasing the length of templates resulted in ex-
 231 cessive phase-overlap and compromised our ability to conduct later phase-picking anal-
 232 ysis of detections.

233 We computed detections between 1 January 2009 and 2 November 2019 using the
 234 EQcorrscan package (Chamberlain et al., 2018) which computes the stack of the normal-
 235 ized cross-correlation between template waveforms and continuous data across multiple
 236 channels. We used the efficient FFTW (Fastest Fourier Transform in the West Frigo and
 237 Johnson (1998)) backend that implements the chunked-correlation algorithm of Senobari
 238 et al. (2019). Detections were made when the summed correlations exceeded $10\times$ the me-
 239 dian absolute deviation of the day-long stack of correlations, and had at least an aver-
 240 age normalized correlation above 0.15. Detections from individual templates were required
 241 to be at least 4 s apart. To remove duplicate detections (e.g. detections of the same event
 242 by different templates), we retained only the detections with the highest average corre-
 243 lation if multiple detections occurred within 1 s of each other.

244 To enable location of the detected events and further remove false detections we
 245 computed cross-correlation derived phase-picks, following the methodology outlined by
 246 Warren-Smith et al. (2017). For each detection, the relevant channel of the template and
 247 continuous data were correlated in a short window of ± 0.5 s around the assumed pick-
 248 time based on a time-shifted version of the template phase-pick. A pick was made at the
 249 maximum of this 1 s-long correlogram, if the maximum normalized correlation exceeded
 250 0.4. Following this step, detections with picks on fewer than five stations were removed.
 251 This provided a catalog of 33,272 events comprising 751,009 phase-picks.

252 Because most of our detections were made during the active aftershock sequence
 253 of the Kaikōura earthquake, some of the correlation picks we made were associated with
 254 the wrong event due to overlapping events from different parts of the aftershock region.
 255 To combat this we undertook an additional quality-control step in which, for each event,
 256 we located the event using HYPOCENTER (Lienert & Havskov, 1995) and the 1D ve-
 257 locity model of Okada et al. (2019). If the root-mean-squared (RMS) travel-time resid-
 258 ual of the location exceeded 1 s the pick with the highest residual was removed and the
 259 event located again. We repeated this process until either the RMS fell below 1 s, or picks
 260 from fewer than five stations remained. If the events RMS did not drop below 1 s with

261 more than five stations, the event was discarded. This removed 30 events leaving us a
 262 total of 33,242 events and 748,641 phase picks.

263 We located the detected earthquakes using the NonLinLoc software of Lomax et
 264 al. (2000) and the New Zealand-wide 3D (NZ3D) velocity model of Eberhart-Phillips et
 265 al. (2017), version 2.2, which includes the updated tomography around the Cook Strait
 266 region conducted by Henrys et al. (2020). We note that the issues encountered by Lanza
 267 et al. (2019) in using NonLinLoc were rectified here by changing a flag in the NonLin-
 268 Loc Grid2Time3D source-code. We also tested using SIMUL2014 (Eberhart-Phillips &
 269 Bannister, 2015) and found that the fit to the data was degraded compared to our Non-
 270 LinLoc locations. We suspect that this reduced quality is because our events frequently
 271 contain S-picks without a corresponding P-pick, which SIMUL2014 cannot use. This is
 272 because S-phases usually correlate better than P-phases due to their high amplitudes.
 273 We were able to locate all events, but only 32,688 events are considered here because 554
 274 occurred outside the study region (Figure 2).

275 Following this location step, we made automatic amplitude picks for all events and
 276 used these to compute local magnitudes. We used the EQcorrscan (Chamberlain et al.,
 277 2018) amplitude-picking routines which pick half the maximum peak-to-trough ampli-
 278 tude on a filtered, Wood-Anderson-simulated trace and correct for the applied filter. Com-
 279 parison of these automatic picks with GeoNet amplitude picks for similar events (both
 280 those within the template set and not in the template set) shows good agreement. We
 281 then computed local magnitudes by inverting for a local magnitude scale that maps to
 282 moment magnitudes, following the methodology of (Michailos et al., 2019), taken from
 283 the moment tensor catalog maintained by GeoNet and based on the work of Ristau (2013).

284 We subsequently undertook relative relocation of all earthquakes using the Grow-
 285 Clust software (Trugman & Shearer, 2017) and HypoDD (version 2.1b) (Waldhauser &
 286 Ellsworth, 2000). For GrowClust we used an average 1D velocity model extracted from
 287 the NZ3D velocity model (between 72–110 km in X and –100–80 km in Y in the coord-
 288 inate system of Eberhart-Phillips and Bannister (2015), Supplementary Table S1) used
 289 for initial location. For HypoDD we used the NZ3D model version 2.2 (Henrys et al., 2020;
 290 Eberhart-Phillips & Bannister, 2015). We found little difference between the two loca-
 291 tion methods, and so report the GrowClust locations here because they provide robust,
 292 bootstrapped uncertainties (Trugman & Shearer, 2017). We were able to relocate 23,684
 293 earthquakes in total.

294 Finally, we computed first-motion-derived focal mechanism solutions for template
 295 events. Because the matched-filter method implicitly requires that detected events have
 296 similar waveforms and hence similar locations and focal mechanisms, we assume that de-
 297 tectations share the same or similar focal mechanism with the template events. Further-
 298 more, our subsequent correlation re-picking enforces that only picks of the same polar-
 299 ity as the template are retained in our final catalog, additionally constraining the detected
 300 focal mechanisms to be similar to the template mechanisms.

301 To compute template focal mechanisms we undertook manual polarity determina-
 302 tion of the automatically determined P arrivals from Lanza et al. (2019). We included
 303 stations from the STREWN network, and strong-motion stations in the GeoNet network
 304 (station locations are plotted in Supplementary Figure S8), but note that we did not use
 305 the timing of these phase arrivals in our location calculations. We then inverted for the
 306 best-fitting focal mechanisms of all template events with polarity picks at more than 10
 307 stations ($n=1,755$) using the Bayesian approach outlined by Walsh et al. (2009). We used
 308 our NonLinLoc derived location estimates and uncertainties to compute takeoff angle
 309 and azimuth posterior density functions.

3 Results

We detected and located 33,242 earthquakes that occurred between 1 January 2009 and 2 November 2019 associated with the regions active during the aftershock sequence of the 2016 Kaikōura M7.8 earthquake. Of these earthquakes, we were able to compute precise relative relocations for a suite of 23,684 earthquakes (Figure 2). Our NonLinLoc locations have median 68% confidence uncertainties of between 2.1 km and 3.7 km (minimum and maximum confidence ellipsoid lengths) and 4.0 km in depth (Supplementary Figure S6). Our GrowClust relocations have median relative uncertainties of 0.4 km in horizontal and depth directions.

As found by Lanza et al. (2019), but not by GeoNet, our hypocentre location for the Kaikōura mainshock lies almost directly beneath the Humps Fault (at a depth of 12.3 km), about 7.7 km NNW from the GeoNet location (beyond the bounds of uncertainties of either location) and c. 2 km north of the location obtained by Nicol et al. (2018). We were not able to relocate the mainshock hypocentre (using Growclust or HypoDD) due to the complexity and clipping of the waveforms and resulting low correlations with other events. This mis-location by GeoNet is likely due to the use of an inappropriate velocity model (ISAP91: <https://www.geonet.org.nz/earthquake/technical/2016p858000> last accessed September 7 2020). We discuss the variation in hypocentre location further in Section 4.1.

We obtain magnitudes ranging from 0.4–6.3 (Figure 3). We note that the maximum magnitude of 6.3 was computed for the M_W 7.8 mainshock, which is beyond the range at which we would expect reliable amplitude-based local magnitudes (see Supplementary Figure S5). The largest aftershock magnitude we calculated is M_L 5.9 30 minutes after the mainshock, for which GeoNet provide a magnitude of M_L 6.2. In general our local magnitude scale gives lower magnitudes than GeoNet at high magnitudes (Supplementary Figure S5). We were unable to calculate magnitudes for 75 earthquakes due to insufficient amplitude picks of sufficient quality. The completeness of our catalog is strongly variable in time: as noted by Hainzl (2016), during periods of high-rate seismicity the magnitude of completeness increases, and we observe this after the Kaikōura mainshock. Before and within a few months after the mainshock, our magnitude of completeness is around M_L 1.2, however in the hours after the mainshock the completeness becomes as elevated as M_L 3.8 (Figure 3). One of the main causes of elevated completeness, despite the ability of the matched-filter method to detect earthquakes with overlapping waveforms, is the restriction in our workflow to only detect events separated by at least 1 s.

The vast majority of earthquakes in our catalog are aftershocks of the Kaikōura earthquake (30,535 events, or 92%, occurred after the mainshock). The earliest aftershock we detect occurred 2 minutes and 45 s after the mainshock origin time, approximately 45–65 s after the completion of the mainshock rupture (Holden et al., 2017). However our catalog also includes aftershocks of the Cook Strait earthquakes, with 2,351 earthquakes between the start of the Cook Strait sequence on the 18th of July 2013 and the Kaikōura mainshock. Some events in our catalog appear to be associated with failure within the subducted plate. The sequence of earthquakes visible in Figure 3 at c. 125 km along the section occur at c. 25 km depth and have focal mechanisms consistent with normal-faulting in the subducted slab. Interestingly this family of earthquakes culminated in a sequence of ten earthquakes in the seven days prior to the Kaikōura mainshock. We also detect limited earthquakes associated with slip on the subduction interface made by templates representing likely interface events reported by Lanza et al. (2019) near Cape Campbell. Most (29,764 or 90% of absolute locations and of 21,620 or 91% relative relocations) of our earthquakes are found to have been shallower than 15 km.

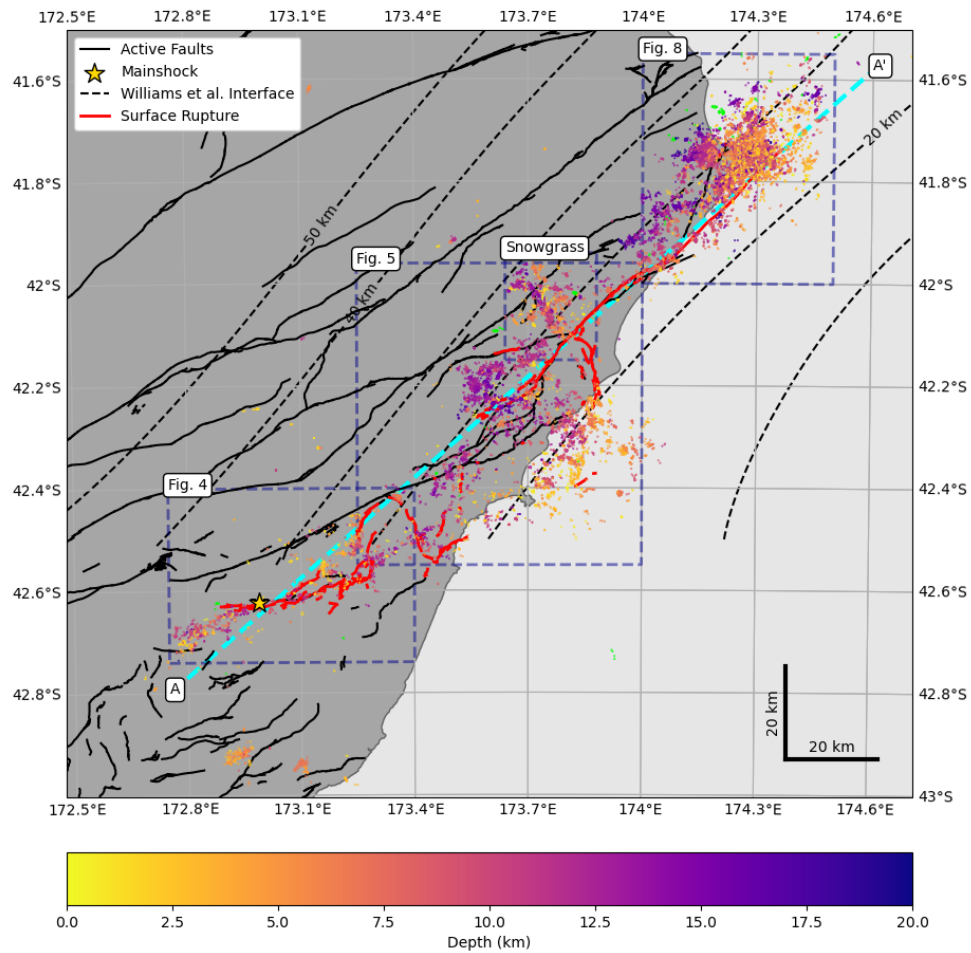


Figure 2. Earthquakes on and around the faults (red lines) that ruptured in the Kaikōura earthquake plotted as circles coloured by depth. Earthquakes deeper than 20 km are plotted in green. Dashed contours mark the depth to the modelled subduction interface (C. A. Williams et al., 2013). The dashed cyan line, labelled A-A' is the cross-section line shown in Figure 7. Dashed dark blue boxes mark the bounds of the relevant figures. The gold star marks the mainshock hypocentre computed here.

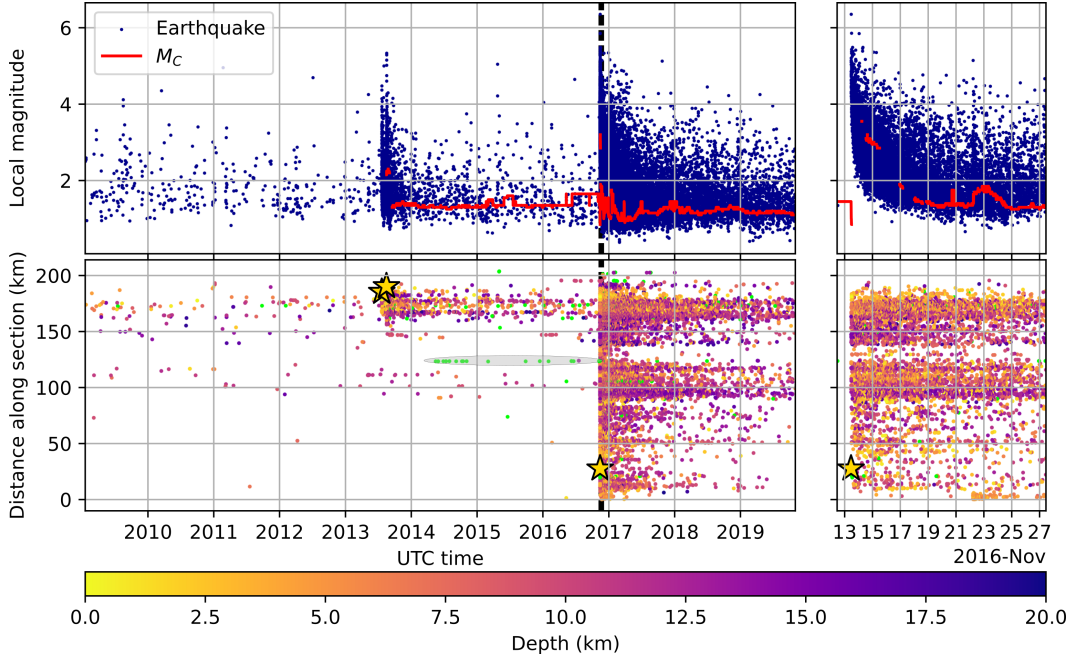


Figure 3. Upper panel: Local magnitudes for all earthquakes in our catalog (blue) and magnitude of completeness computed by goodness-of-fit (Wiemer, Stefan and Wyss, Max, 2000) (red). Magnitude of completeness was computed using a sliding window of 1,000 events. Magnitude of completeness is only shown when at-least 300 magnitudes were above the best fitting completeness, and the fit was above 98%. Lower panel: Earthquakes projected onto the A-A' cross-section (Figure 2), and plotted against origin-time. Earthquakes are coloured by depth. Earthquakes deeper than 20 km are plotted in green and the grey ellipse outlines the deep normal-faulting sequence discussed in the text. The Lake Grassmere, Cook Strait and Kaikōura earthquakes are plotted as gold stars. Right panels show zoomed in views of the two weeks following the Kaikōura mainshock, marked as vertical dashed black lines in the left panels.

4 Discussion

This updated and expanded catalog of earthquakes on and surrounding the faults that ruptured in the Kaikōura earthquake serves as the basis to re-evaluate some of the outstanding questions regarding this complex earthquake. Here we discuss the key questions outlined previously and highlight some key fault structures that have previously been poorly resolved or unknown.

4.1 Rupture Initiation

Multiple hypocentre locations for the Kaikōura earthquake are now available and, as demonstrated by Nicol et al. (2018), there is some inconsistency between them. In our locations we find that the mainshock hypocentre locates almost directly beneath the surface trace of the Humps Fault, at a depth of 12.9 ± 4.5 km (Figure 4). The first-motion-derived focal mechanism of the mainshock that we construct here (strike/dip/rake of $246^\circ/80^\circ/174^\circ$) is consistent with dextral slip on a steeply dipping plane similar to the strike of the Humps Fault. A Gaussian fit to the NonLinLoc uncertainties at the 1σ level provides a horizontal uncertainty ellipse oriented at 105° with a maximum length of 2.2 km and minimum length of 1.8 km. Our location is slightly different (but within uncertainty) from that of the previous solution of Lanza et al. (2019), whose phase picks we use here, and notably different from the Geonet location that does not place the hypocentre on the Humps Fault. The GeoNet hypocentre could indicate that an initial rupture on a separate fault to the south occurred, which subsequently triggered slip on the Humps Fault as suggested by Ando and Kaneko (2018) to explain some of the mismatch in the initial rupture speed between their model and observations. However, we are confident that the rupture did in fact nucleate on the Humps Fault, and discuss possible causes of the discrepancies in locations below.

In this work we have not used picks on the strong-motion sites with known timing problems. We also use an updated velocity model, and a different location method compared to Lanza et al. (2019). When we use the same location method (using the software SIMUL) and/or use the same velocity model as Lanza et al. (2019), we obtain a similar result to our preferred solution, suggesting that the main source of error in the previous location of Lanza et al. (2019) was from the inclusion of picks from sites with problematic timing.

The GeoNet preferred location for the mainshock hypocentre (at the time of writing this, 24 April 2021, was at -42.693° N, 173.022° E and 15.11 km depth) lies 7.7 km to the south of our location, beyond the combined uncertainties in our location and the quoted horizontal uncertainty in the GeoNet location (2.3 km in latitude and 3.4 km in longitude). The GeoNet solution is computed using the IASP91 (Kennett & Engdahl, 1991) global 1D velocity model and the LOCSAT location program (Bratt & Nagy, 1991). When we locate the mainshock using the GeoNet pick times in NonLinLoc using the NZ3D 2.2 velocity model used here we obtain a similar location to our location (within uncertainty). We suggest that the use of the global 1D velocity model is inappropriate for accurate location of crustal seismicity in New Zealand, and results in incorrect locations and under estimated location uncertainties. Similar issues are likely to apply to other location solutions for the Kaikōura mainshock that do not use an appropriate velocity model.

The location computed by Nicol et al. (2018) is within the uncertainty of our location, and was computed using a similar method to that used here. However, the aftershock relocations computed by Nicol et al. (2018) use GeoNet locations as starting locations, which are inaccurate due to the use of the IASP91 velocity model. As such, relocation from these inaccurate starting locations is the likely cause of difference between the relocations of Nicol et al. (2018) and those presented here, which here delineate a nearly vertical structure consistent with our mainshock focal mechanism. The south-dipping

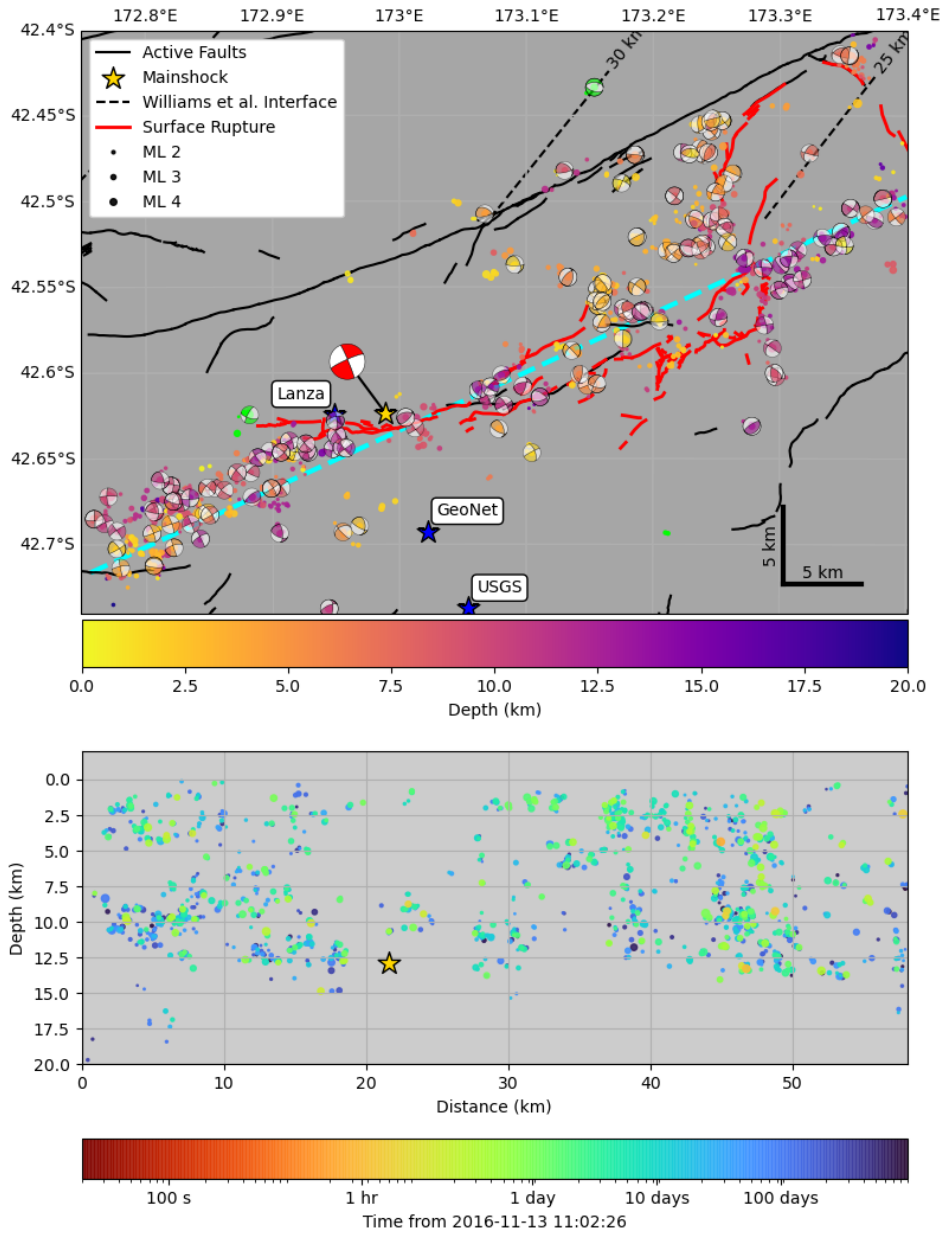


Figure 4. Nucleation region of the Kaikōura earthquake. Upper panel: map of relocated earthquakes (circles coloured by depth and scaled by magnitude) and focal mechanisms of template events, coloured by depth. Earthquakes deeper than 20 km are plotted in green. Mainshock location is marked by a star: note that this is an absolute location rather than a relocation for reasons explained in the text. The first-motion derived focal mechanism of the mainshock is shown in red. Alternative mainshock locations are plotted as blue stars and labelled as Lanza, GeoNet and USGS for the Lanza et al. (2019), GeoNet and USGS solutions respectively. Mapped surface ruptures are plotted as red lines, and other faults of the NZ active faults database are plotted in black. Dashed black contours mark the modelled subduction interface from C. A. Williams et al. (2013). The dashed cyan line shows the cross-section line plotted in the lower panel. Lower panel: Cross-section (SW to NE) of relocated hypocentres projected onto the cyan line in the upper panel. Earthquakes are coloured by time since 30s prior to mainshock, note that the colour scale is logarithmic. Earthquakes are scaled by magnitude. The star marks the absolute location of the mainshock.

408 lineation extending through the subduction interface shown by Nicol et al. (2018) is not
409 visible in our relocations, probably due to more robust starting locations used here.

410 We note that a foreshock c. 7 s prior to the mainshock (Supplementary Figure S1)
411 may also have contributed to inaccuracies in mainshock location: if picks were made on
412 the much smaller foreshock P-phases for the four GeoNet stations that they are visible
413 on then these arrival times would bias the location. This foreshock is located close to
414 the mainshock, but the mainshock obscures the S-phase on most stations and the P-phase
415 is only visible on four stations due to the size of the foreshock, and the resulting loca-
416 tion we obtain has high uncertainties. We did not detect this foreshock with out matched-
417 filter detector due to the poor signal on most stations, and it is therefore not included
418 in our catalog.

419 In summary, our more accurate mainshock location and focal mechanism confirm
420 that the Kaikōura earthquake most likely nucleated as a dextral strike-slip rupture of
421 the Humps Fault, and confirm that the Humps Fault here is steeply dipping (c. 80°) to
422 the North. This suggests that off-fault triggering did not play a strong role in the nu-
423 cleation of the Kaikōura earthquake, and other factors must be the cause of the early
424 long-duration release of seismic energy. Ulrich et al. (2019) were able to reproduce the
425 slow initial phase of the rupture through the Humps–Hundalee system in their dynamic
426 rupture simulation. Finally, it is worth noting that any seismic backprojections that com-
427 pute the location of high-frequency radiation sources relative to the mainshock may be
428 biased by the use of inaccurate hypocentres (e.g. Tan et al., 2019; D. Wang et al., 2018).

429 We do not observe precursory seismicity aside from the foreshock approximately
430 7 s prior to the mainshock. This includes no seismicity in the epicentral region follow-
431 ing any of the 2010 Darfield earthquake, 2011 Christchurch earthquakes, or the 2013 Cook
432 Strait sequence, which are likely to have induced dynamic stress changes in the epicen-
433 tral region of the Kaikōura earthquake. We attempted to run a focused matched-filter
434 search using GeoNet data and the 7 s foreshock as a template, but this did not make any
435 further reliable detections.

436 4.2 Rupture Pathway

437 The Kaikōura earthquake involved substantial rupture (>1.5 m surface slip) of at
438 least 13 faults (Litchfield et al., 2018). Initial observations suggested that large stepovers
439 (up to 20 km), particularly between the southern faults (Humps–Hundalee system) and
440 the high slip Kekerengu Fault, were present (Kaiser et al., 2017; Hamling et al., 2017).
441 Such large stepovers commonly correspond to rupture termination points (Wesnousky,
442 2006; Harris et al., 1991). More recently, additional faults, including the Point Keen or
443 other offshore reverse faults, and/or links between the Hundalee and Jordan Thrust/Upper
444 Kowhai Faults (via the Leader and Whites Faults) have been postulated to explain the
445 rupture sequence (e.g. Ando & Kaneko, 2018; Zinke et al., 2019). In particular, the dy-
446 namic rupture model of Ando and Kaneko (2018) has rupture propagating from the Hun-
447 dalee Fault to the Upper Kowhai and Jordan Thrust Faults with limited slip on the link-
448 ing Whites Fault (Figure 6), and suggests that this step-over was accommodated mostly
449 by transient dynamic stresses or elastic waves. In contrast, the dynamic rupture model
450 of Ulrich et al. (2019) has rupture propagating from the Hundalee Fault onto the offshore
451 reverse faults before triggering slip on the Papatea Fault, which then caused rupture of
452 the Jordan Thrust and Kekerengu Faults.

453 Our earthquake locations help to illuminate the structure of these linking faults
454 at depth (Figure 5). Two key faults emerge: (1) an offshore, dominantly reverse, struc-
455 ture similar to the Point Keen Fault modelled by Ulrich et al. (2019); Hamling et al. (2017)
456 and (2) a previously unidentified strike-slip, near-vertical structure linking the Papatea-
457 Jordan Thrust-Kekerengu-Fidget junction to the inland, unruptured Clarence Fault. We
458 herein refer to this new second fault as the Snowgrass Fault, named after a nearby stream.

459 Note that this fault is not associated with any reported surface rupture. There is also
 460 a continuous trend of earthquake locations spanning the gap between the southern fault
 461 system and the Jordan Thrust, suggesting that either the offshore route, via the offshore
 462 thrust system, or the onshore route, via the Whites Fault are viable options for rupture
 463 propagation.

464 Several key observations provide further constraints on the most likely rupture route
 465 for the Kaikōura earthquake, principally the occurrence of a small, localised tsunami (Gusman
 466 et al., 2018), and the inverted motion of the Jordan Thrust, which hosted normal mo-
 467 tion rather than the reverse motion, as would be expected from the geological record (Howell
 468 et al., 2020; Van Dissen & Yeats, 1991). We propose that these two factors, alongside
 469 our observation that offshore thrust faulting spans the gap between the Hundalee Fault
 470 and the Papatea Fault, require that the earthquake propagated via the offshore route
 471 (Figure 6). In addition the observation of a tsunami requires some co-seismic offshore
 472 deformation which would be provided by offshore thrust faulting (Gusman et al., 2018),
 473 and the normal (inverted) sense of slip on the Jordan Thrust Fault can be explained by
 474 our preferred model. This is in agreement with recent modelling studies by Ulrich et al.
 475 (2019) and Klinger et al. (2018).

476 In our preferred rupture scenario we suggest that the offshore thrust fault (or faults,
 477 here labelled as the Point Keen Fault for consistency, despite the opposite sense of slip
 478 compared to the geologically recognised Point Keen Fault (Litchfield et al., 2018)), the
 479 Papatea Fault, and extending into the newly discovered Snowgrass Fault acted as one
 480 thrust block with a sinistral north-western edge (Figure 6). Within this thrust block, the
 481 normal motion of the usually reverse Jordan Thrust Fault occurs as a consequence of the
 482 eastward motion of eastern side of the block (normally the footwall). In other words, the
 483 coastal side of the Jordan Thrust is extended seawards relative to the pinned inland side
 484 resulting in normal motion.

485 This scenario can also help explain the high slip on the Papatea Fault. In this sce-
 486 nario, the Papatea Fault sits at the corner between dominantly thrust motion offshore,
 487 to dominantly sinistral-normal oblique motion onshore on the Snowgrass Fault. Not only
 488 does this scenario provide additional fault length for the combined Papatea-Snowgrass-
 489 Point Keen Fault system, meaning that co-seismic displacements scale more consistently
 490 with fault length, but also that the Papatea Fault acts in a similar style to a restrain-
 491 ing bend, e.g. with large co-seismic strain exceeding the long-term accumulated elastic
 492 strain, which other authors have suggested is insufficient to explain the slip amplitude
 493 on the Papatea Fault (e.g. Diederichs et al., 2019).

494 We use the same equations, converted to SI units, as R. M. Langridge et al. (2018),
 495 after Stirling et al. (2012), namely:

$$M_W = 2/3 \log W + 4/3 \log L - 1.82, \quad (1)$$

496 where W is fault width and L is fault length, both in meters, and

$$M_0 = \mu L W D, \quad (2)$$

497 where M_0 is the seismic moment in Nm, μ is the shear modulus, which Stirling et al. (2012)
 498 assume to be 3×10^{10} Pa², L and W are as before, and D is the single-event displace-
 499 ment in meters. M_0 is calculated using:

$$\log M_0 = 9.05 + 1.5 M_W. \quad (3)$$

500 This way, we are able to estimate single-event displacements for various fault combina-
 501 tions. We deduce that R. M. Langridge et al. (2018) adopted a fault width of 18.5 km
 502 based on the magnitude they compute. Using this fault width and a combination of the
 503 Papatea and Snowgrass faults (which adds approximately 15 km to the length) we find

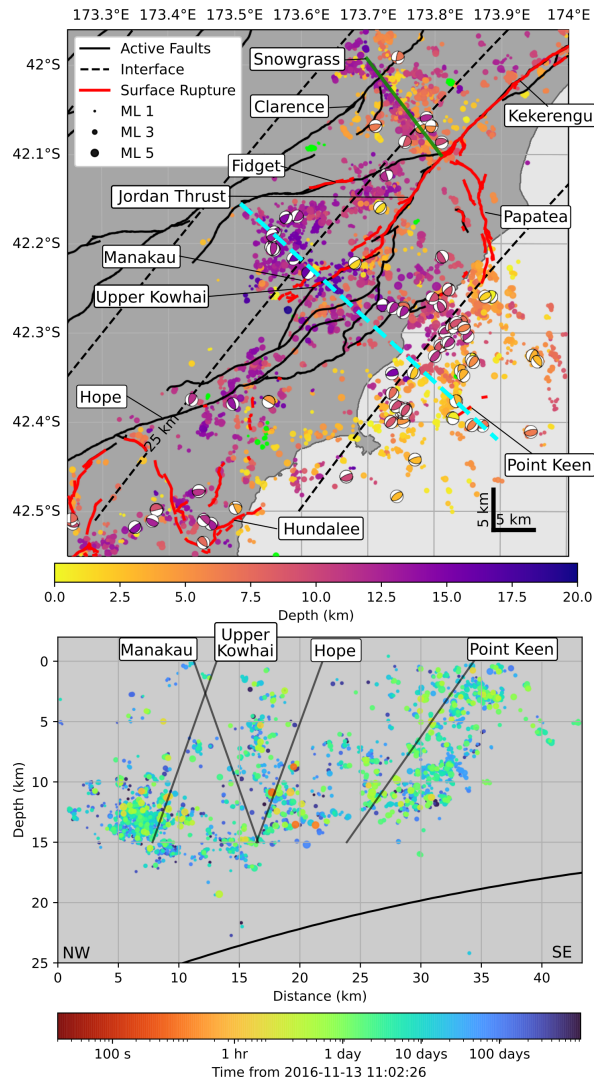


Figure 5. Earthquake locations around the transition from southern/epicentral faults to the Kekerengu fault. Top: map view of relocated earthquakes plotted as circles coloured by depth and scaled by magnitude. Earthquakes deeper than 20 km are plotted in green. Thrust focal mechanisms ($45^\circ < \text{rake} < 135^\circ$) for template events are also plotted, coloured by depth. Active faults are plotted in black, and faults with known surface rupture during the Kaikōura earthquake are plotted in red. Black dashed contours mark the depth to the interface model of C. A. Williams et al. (2013). The cyan dashed line marks the cross-section line shown in the lower panel. The green solid line marks the inferred location of the newly identified Snowgrass fault (labelled). Note that the surface dip of the Clarence Fault is c. 70° NW (Rattenbury & Isaac, 2012), and the Snowgrass fault appears to terminate at the Clarence Fault at depth. Bottom: Cross-section perpendicular to the dominant strike of reverse focal mechanisms. Earthquakes within 7.5 km of the cross-section are projected onto the line. Solid straight lines mark the locations and dips of cross-section intersecting faults from Litchfield et al. (2018). The solid curved line at depth marks the subduction interface model of C. A. Williams et al. (2013). Note that the broad cluster of earthquakes at the down-dip end of the Upper Kowhai Fault is likely associated with projecting earthquakes on a fault striking obliquely to the cross-section. Similarly, our preferred arcuate geometry of offshore thrusting, and variable dip provides an explanation for the broad region of earthquakes below the inferred Point Keen Fault.

504 a single-event displacement of 2.3 m. Incorporating the Point Keen Fault in our preferred
 505 geometry results in an 83 km total length and average displacement of 5.8 m. Finally, in-
 506 cluding the section of the Hundalee Fault between the coast and the Stone Jug Fault in-
 507 creases the length to 93 km and slip to 6.5 m. The average net slip on the Papatea Fault
 508 was measured to be 6.4 ± 0.2 (R. M. Langridge et al., 2018), reinforcing our proposed com-
 509 bined fault system explanation.

510 The existence of the Snowgrass Fault also helps to explain the drop in slip across
 511 the Kekerengu-Jordan Thrust junction, despite the similar strikes of these two faults.
 512 A simple model of this junction is that of a quadruple junction between the Jordan Thrust,
 513 Papatea, Kekerengu and Snowgrass Faults (discounting the Fidget Fault that has mapped
 514 surface rupture away from the junction, but not nearby (Litchfield et al., 2018)). By av-
 515 eraging the InSAR derived coseismic displacement field (Hamling, 2020) in blocks around
 516 the fault system (see Supplementary Figures S2 and S3) we estimate the strike-parallel
 517 and perpendicular components of motion on the Snowgrass to be 1.3 m sinistral and 3.4 m
 518 of extension. The resulting sinistral transtensional motion is consistent with the dom-
 519 inant aftershock focal mechanisms (Supplementary Figure S8). The strong change in the
 520 InSAR-derived North-South displacement field aligns with the strike of the Snowgrass
 521 Fault constrained by our earthquake locations.

522 Including the Snowgrass Fault as a separation between the western side of the Kek-
 523 erengu Fault and the western (inland) side of the Jordan Thrust reduces the required
 524 dextral motion from 6.2 m on the Kekerengu to 3.3 m on the Jordan Thrust. The dif-
 525 ference in these estimated offsets corresponds well with the difference in dextral offsets
 526 measured by Kearsse et al. (2018), which rise from c. 1–8 m on the Jordan Thrust, and
 527 are generally between 10–12 m on the Kekerengu Fault (see Supplementary Figures S2
 528 and S3). Without the Snowgrass Fault, block offsets require 5.1 m and 5.0 m of dextral
 529 slip on the Kekerengu and Jordan Thrust Faults, which does not allow for change in the
 530 change in dextral offset observed. Our estimates do not capture the total slip on the faults
 531 because we use spatially averaged displacements in off-fault blocks to capture the gen-
 532 eral kinematics. Nevertheless, the change in slip between the Kekerengu and Jordan Thrust
 533 cannot be accommodated without some additional deformation, and the Snowgrass Fault
 534 provides a viable structure for this deformation.

535 We suggest, therefore, that the Kaikōura earthquake propagated from the Hundalee
 536 Fault onto the offshore thrust system, which then activated the Papatea and Snowgrass
 537 Faults, which in turn triggered slip on the Kekerengu Fault. In this model, the role of
 538 the Jordan Thrust is minor, and the extension of aftershocks between the Jordan Thrust
 539 to the Whites Fault is a consequence of the underlying thrust system. This scenario agrees
 540 with the dynamic rupture simulation of Ulrich et al. (2019), but is at odds with that of
 541 Ando and Kaneko (2018) whose model did not result in significant slip on the Papatea
 542 Fault. We note that both Ando and Kaneko (2018) and Ulrich et al. (2019) have used
 543 a shallower dip on the offshore thrust system than the $45\text{--}60^\circ$ dip found here, which re-
 544 sults in a reduced possible stress-drop in the model of Ando and Kaneko (2018), mak-
 545 ing it a less favourable rupture pathway in their model.

546 The Snowgrass Fault also appears to link with the Clarence Fault, a key compo-
 547 nent of the Marlborough Fault system (Van Dissen & Nicol, 2009) that did not rupture
 548 in the Kaikōura earthquake. One of the earliest aftershocks we detected, a $M_L 4.8$ within
 549 nine minutes of the mainshock origin time, occurred at the junction of the Snowgrass
 550 and Clarence Faults, suggesting that the Clarence Fault may have been active early in
 551 the aftershock sequence. That neither the Hope nor the Clarence Faults had significant
 552 co-seismic rupture despite evident triggered aftershocks, remains an intriguing observa-
 553 tion.

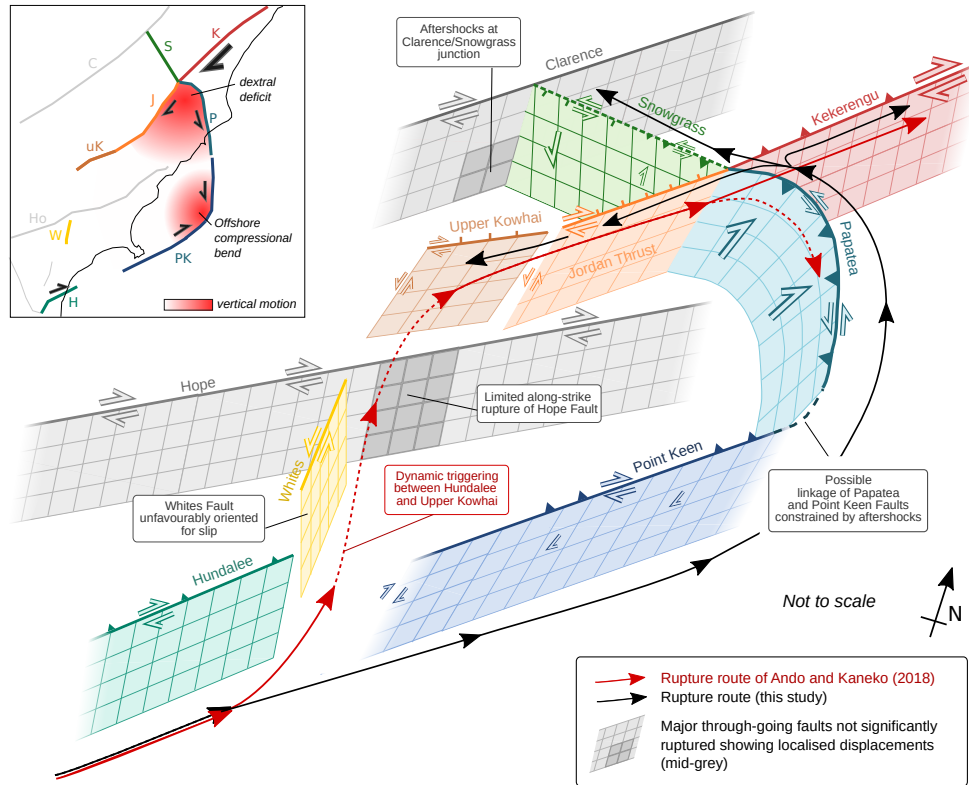


Figure 6. Schematic, not-to scale cartoon illustrating links between faults in the stepover region between the southern faults and the high slip Kekerengu Fault, and how the Papatea Fault may operate as a restraining pop-up. Faults in grey represent major through-going structures of the Marlborough Fault Zone (the Hope and Clarence Faults) which did not have significant co-seismic rupture, but which may have localised slip at depth near fault junctions as indicated by darker grey shading. Coloured, outlined arrows on faults show sense of co-seismic motion, approximately scaled by size to show relative slip magnitudes between different faults. The thin red line with arrows shows preferred inland rupture route of Ando and Kaneko (2018) via the Whites Fault (inferred, dashed line) and triggered slip on the Papatea (also denoted by dashed line). The thin black line with arrows shows our preferred offshore rupture route, with bi-lateral rupture originating from the Papatea-Kekerengu-Snowgrass-Jordan Thrust junction. Inset shows simplified map view of faults, coloured as in main plot, illustrating how the Papatea-Point Keen connection forms an offshore compressional bend with anticipated vertical motion.

554

4.3 Subduction Interface

555

556

557

558

559

560

561

562

563

We observe no earthquakes consistent with slip on the subduction interface beneath the majority of the upper-plate faults (Figure 7). The few earthquakes observed close to the subduction interface (e.g. at 23 km depth in Figure 5) show normal-faulting mechanisms, consistent with extension in the down-going plate, and were active prior to the Kaikōura earthquake. Some earthquakes consistent with subduction interface slip occur beneath the Cape Campbell region, as shown by Lanza et al. (2019) and here (Figure 8), but not all show mechanisms consistent with interface slip here. It may be that the northern-tip of South Island is the point where the subduction interface becomes seismically active, as proposed by Henrys et al. (2020).

564

565

566

567

568

569

570

571

572

When considering the significance of a lack of aftershocks in our catalog on the subduction interface it is important to restate the limitations of matched-filter catalogs. Such catalogs by definition only contain earthquakes similar to those in the template dataset: if we do not have any subduction interface earthquakes in our template set then we should not be surprised to see no subduction related events in the final catalog. However, our template catalog is composed of all earthquakes in the GeoNet catalog between 13 November 2016 and 13 May 2017 larger than $M_L 3$ (Lanza et al., 2019). As such, any missing seismicity should be of small magnitude and therefore likely contributed minimally to the total (post-seismic) moment release.

573

574

575

576

577

578

579

580

Our dataset provides no direct constraints on whether the subduction interface slipped co-seismically, but by more accurately mapping crustal seismicity we are able to robustly demonstrate the existence of offshore thrust faulting south of the Kekerengu Fault. Such offshore faulting has been previously used in models that recreate co-seismic data without the need for significant slip on a subduction source (e.g Gusman et al., 2018; Clark et al., 2017). Incorporating more realistic models of crustal faulting at depth, derived from our catalog, may provide greater constraints on the co-seismic role of the subduction interface.

581

582

583

584

585

586

587

588

The lack of aftershocks on the subduction interface does not preclude afterslip on the interface because this afterslip could be aseismic. However, it seems unlikely that if the subduction interface is aseismic in the post-seismic period that it would have contributed significantly to the co-seismic seismic wavefield. The published models of post-seismic slip have used simple models of crustal faulting (for instance Wallace et al. (2018) use four crustal fault sources attempting to simulate the Humps, Kekerengu/Jordan Thrust, Needles and an offshore thrust fault). The simplicity in crustal faults may lead to inaccurate mapping of slip onto the underlying subduction interface.

589

590

591

592

593

594

595

596

597

598

599

600

601

602

603

604

For example, in the Cape Campbell area, at the northern tip of South Island, strong co- and post-seismic uplift occurred (Wallace et al., 2018). This uplift includes a large short-wavelength component: the uplift at GNSS station CMBL is more than triple that at station WITH (Figures 1 and 9), within a few tens of kilometres. WITH and CMBL are separated by the faults that ruptured in the Lake Grassmere earthquake (Hamling et al., 2014), which were re-invigorated during the Kaikōura aftershock sequence (Figure 8). These faults are more shallowly dipping than the Needles Fault, and have a significant reverse component (Hamling et al., 2014), but the pattern of uplift observed in the Kaikōura earthquake is the reverse of that in the Lake Grassmere earthquake (Hamling et al., 2014). This suggests that either the Lake Grassmere and Cook Strait Faults were reactivated with a normal sense of motion (but we do not observe normal focal mechanisms in this region), or other reverse faults dipping to the East, such as the London Hills Fault, were responsible for this short-wavelength uplift. No faults between WITH and CMBL with this sense of motion were included in the afterslip model of Wallace et al. (2018). Inclusion of these faults, which have a strong aftershock signature (Figure 8) may reduce the need for interface slip beneath Cape Campbell.

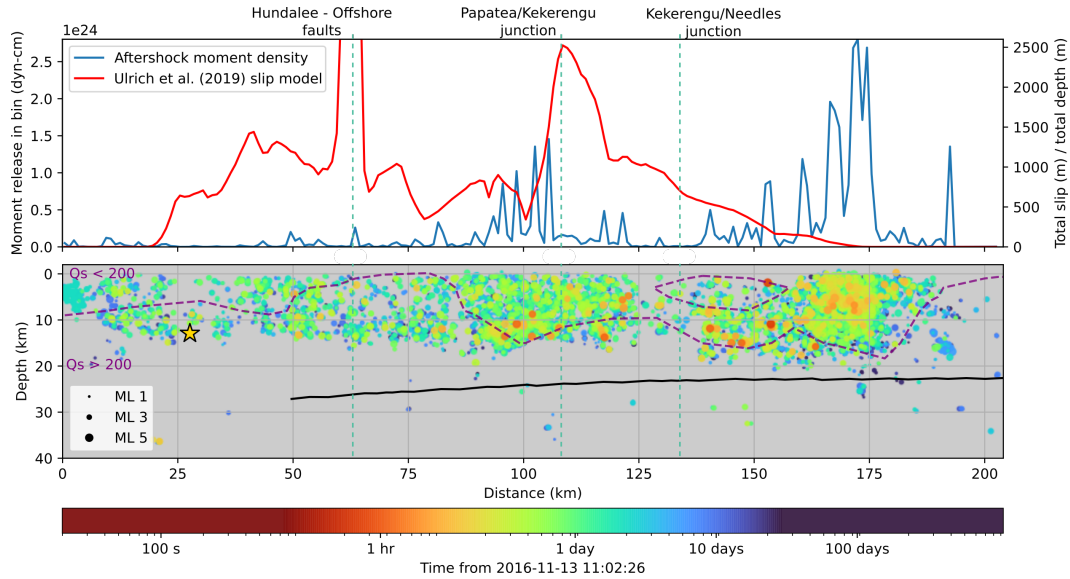


Figure 7. Along-strike earthquake distribution, along line A-A' shown on Figure 2. Top: Aftershock moment density (blue) computed in 1 km bins perpendicular to the cross-section, and slip density derived by Ulrich et al. (2019) (red). Note that the projection of all slip in this 3D fault geometry onto a single plane results in the summation of slip across multiple fault strands. The peak in slip around 65 km along the section occurs at the corner between the Stone Jug and Hundalee faults and is likely unrealistic, and in part due to the projection of slip on a single plane. Bottom: Aftershock locations coloured by time since 30 s prior to the the Kaikōura mainshock. Note that the colour-scale is logarithmic. The location of the epicentre of the mainshock is shown by a gold star, and the depth of the interface from C. A. Williams et al. (2013) is shown as a solid line. The purple dashed contour marks the $Q_s=200$ contour from the NZW3D 2.2 model (Henry et al., 2020).

605 Incorporating more realistic and complex crustal faulting is unlikely to completely
 606 remove the need for slip on the underlying subduction interface: crustal faults are likely
 607 to help to explain short-wavelength geodetic features, but not the long-wavelength fea-
 608 tures seen in both the post-seismic InSAR and GNSS data (Wallace et al., 2018).

609 4.4 Termination

610 The Kaikōura earthquake terminated near Cape Campbell, at the north-eastern
 611 tip of South Island. Surface ruptures were mapped on the Needles (offshore, but with-
 612 out rupture of the nearby/adjoining Boo Boo Fault (Kearse et al., 2018)), Marfells Beach,
 613 Cape Campbell Road and Lighthouse Faults (Litchfield et al., 2018). The rupture ter-
 614 minated despite the existence of multiple other pre-existing mapped faults in the region.
 615 The Cape Campbell region also hosted the 2013 Cook Strait earthquake sequence, in-
 616 cluding the $M_W 6.6$ Cook Strait earthquake on 21 July 2013, and the subsequent $M_W 6.6$
 617 Lake Grassmere earthquake on 16 August 2013 (Hamling et al., 2014). This region is also
 618 close to the modelled southern rupture extend of the $M 8$ 1855 Wairarapa earthquake
 619 (Darby & Beanland, 1992; Rodgers & Little, 2006).

620 Dynamic rupture simulations have been able to simulate arrest on the Needles Fault
 621 (Ulrich et al., 2019; Ando & Kaneko, 2018), either by invoking a small (10° clockwise)
 622 rotation in the regional stress field (Ando & Kaneko, 2018), or by enforcing reduced pre-

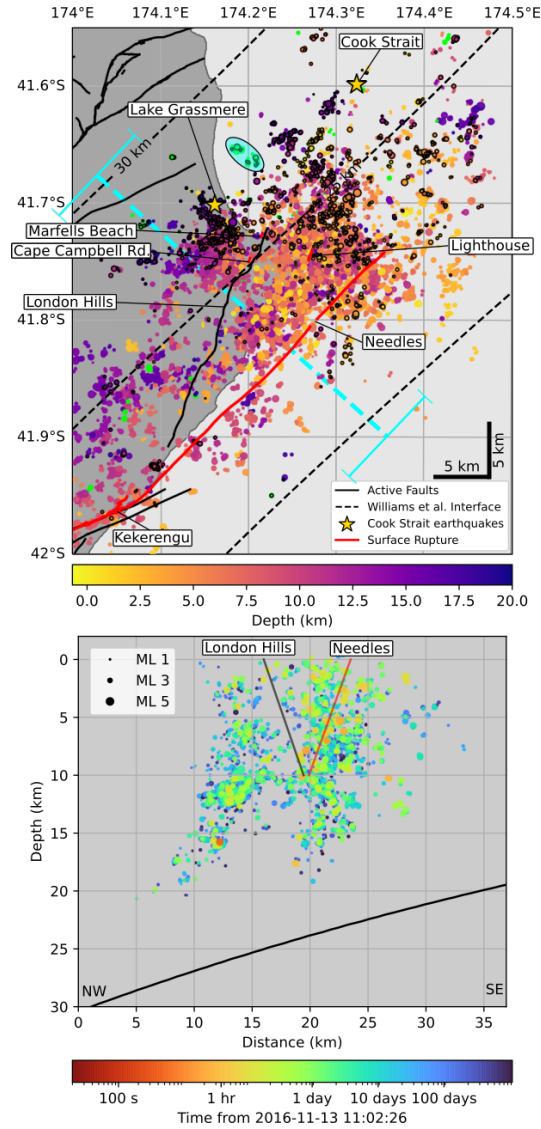


Figure 8. Earthquake locations near the termination of the Kaikōura earthquake. Top: Map view of earthquake relocations coloured by depth. Earthquakes deeper than 20 km are coloured green. Earthquakes with black outlines mark events that occurred prior to the Kaikōura mainshock, including events triggered by the Cook Strait and Lake Grassmere earthquakes in 2013, which are plotted as gold stars. Active faults without surface rupture from the Kaikōura earthquake are plotted as black lines, and those with surface rupture are plotted in red. Black dashed contours show the model of the Hikurangi subduction interface from C. A. Williams et al. (2013). The teal oval outlines the events close to the subduction interface that have mechanisms possibly related to slip on the interface as identified by Lanza et al. (2019). The dashed cyan line marks the cross-section plotted below, and the width of the swath (10 km) is shown at each end of the cross-section line. Bottom: Cross-section of earthquake locations coloured by time after 30 s prior to the Kaikōura mainshock within 5 km of the cross-section line. The subduction interface is shown as a curved solid black line, and the projections of the Needles (surface dip of 70°, (Litchfield et al., 2018)) and London Hills (surface dip of 70° (R. Langridge et al., 2016)) faults to 10 km depth are shown.

623 stress on the Needles Fault while rotating the stress field in the opposite direction (Ulrich
 624 et al., 2019). The two shallow (<25 km) S_{Hmax} estimations from Townend et al. (2012)
 625 in the region (their clusters 16 and 11) suggest a possible clockwise rotation as used by
 626 Ando and Kaneko (2018). The counter-clockwise rotated cluster in Cook Strait (clus-
 627 ter 18) has a centroid at 42 km depth and is likely related to stresses associated with sub-
 628 duction interface beneath. We therefore favour a clockwise rotation to an S_{Hmax} orien-
 629 tation of c. 110° which reduces the potential stress drop on the Needles Fault and leads
 630 to the spontaneous termination in the model of Ando and Kaneko (2018). This rotation
 631 is also consistent with the earlier work of Balfour et al. (2005).

632 Neither of the above-mentioned dynamic rupture models (Ando & Kaneko, 2018;
 633 Ulrich et al., 2019) includes slip on other faults around Cape Campbell, despite the mapped
 634 surface ruptures (Litchfield et al., 2018) and the diffuse aftershocks mapped here and by
 635 Lanza et al. (2019). Importantly, the inferred rupture plane of the Cook Strait earth-
 636 quakes is rotated c. 9° clockwise of the average strike of the Needles Fault (Hamling et
 637 al., 2014), resulting in a more favourable orientation for slip on these faults in the regional
 638 stress-field. Interestingly we see a general paucity of earthquakes on the Needles Fault
 639 (Figure 8) compared to faults directly beneath Cape Campbell. We suggest that this may
 640 be due to the unfavourable orientation of this fault. We also favour a more steeply dip-
 641 ping (near-vertical) Needles Fault, with much of the reverse component of deformation
 642 taken up by shallower dipping faults to the West.

643 Because the templates we use, despite having been constructed exclusively from
 644 aftershocks of the Kaikōura earthquake, detect aftershocks of the Cook Strait sequence
 645 (but not the mainshocks), the Kaikōura aftershock sequence must include re-rupture of
 646 favourably oriented faults that were active during the Cook Strait aftershock sequence.
 647 Focal mechanisms of aftershocks in this region include multiple dextral-reverse mecha-
 648 nisms striking c. 055° , similar to the Cook Strait mainshocks.

649 We consider two possibilities for the cause of the activation of the Cook Strait se-
 650 quence fault(s) by the Kaikōura earthquake: (1) the Kaikōura earthquake co-seismically
 651 ruptured the more favourably oriented “Cook Strait Fault”; (2) seismicity on the “Cook
 652 Strait Fault” was triggered post-seismically. As computed by Ulrich et al. (2019), the
 653 Coulomb failure stress (ΔCFS) reduction on the Needles Fault due to the Cook Strait
 654 sequence is small (c. 0.1 MPa). However, the stress drops on the “Cook Strait Fault” it-
 655 self due to the Cook Strait and Lake Grassmere earthquakes are 1 MPa and 3.5 MPa re-
 656 spectively. We hypothesise that this resulted in reduced pre-stress on the “Cook Strait
 657 Fault”, ensuring that the Kaikōura earthquake could not generate significant rupture through
 658 this more favourably oriented fault, either co-seismically or post-seismically.

659 Our aftershock locations do not show clear evidence for a structural boundary within
 660 Cook Strait as the control for rupture termination. Instead we observe a consistent mi-
 661 gration of aftershocks away from the inferred rupture termination point into Cook Strait
 662 (see section 4.5, Figure 7 and Supplementary Figure S9). Nevertheless, the aftershocks
 663 do concentrate within the region of low Q (high seismic attenuation), as demonstrated
 664 by Henrys et al. (2020). (Henrys et al., 2020) suggested that the change in seismic prop-
 665 erties in Cook Strait may be linked to changes in interface coupling, upper-plate defor-
 666 mation and strain-accumulation, which may play a role in rupture termination. In gen-
 667 eral the aftershocks are found to have occurred within regions of low Q , which may be
 668 indicative of regions of higher fracturing or damage, more capable of hosting seismicity
 669 (Henrys et al., 2020).

670 We suggest that a combination of an unfavourably oriented Needles Fault, reduced
 671 pre-stress due to prior rupture of other nearby faults, and the presence of diffuse fault-
 672 ing around Cape Campbell, served to terminate the rupture near Cape Campbell.

673

4.5 Post-seismic

674

675

676

677

678

679

680

681

682

683

684

685

The catalog we present here is dominated by aftershocks providing important information on deformation processes following complex co-seismic slip. Spatially, several key features are apparent in the post-seismic period (Figure 7). Firstly, the peak aftershock densities occur at the rupture termination point near Cape Campbell, and in the step-over region between the southern and northern rupture domains. Strong aftershock activity near rupture terminations where there are elevated stress concentrations is common (King et al., 1994), but we do not see many aftershocks associated with the Needles Fault (Figure 8): rather, the majority of aftershocks around Cape Campbell occur in a distributed region between the Needles Fault and the location of the 2013 Cook Strait sequence. The patch of aftershocks around Cape Campbell expands in time, following a roughly log-time expansion, and seems to expand bilaterally (Figure 7, Supplementary Figure S9).

686

687

688

689

690

As previously reported, there are very few aftershocks associated with the Papatea Fault and the highest-slip patch of the Kekerengu Fault, which we interpret to be segments that experienced near-total stress-drop. The high-slip patch of the Kekerengu Fault separates the two regions of high aftershock density and may provide a limiting control to the aftershock sequence.

691

692

693

694

695

In the south, we see a continuation of aftershocks beyond the southern rupture termination point, and clustered triggered off-fault seismicity. We also note that, although there are aftershocks on the Leader and surrounding faults, we also see a continuous trend of aftershocks joining the Humps and Hundalee Faults, effectively cutting off this block, and potentially accommodating block rotation as proposed by T. Wang et al. (2020).

696

697

698

699

700

701

702

703

704

705

706

Comparison of GNSS displacements with earthquake rates in regions surrounding the GNSS site shows that aftershock rates are generally proportional to displacement rates (Figure 9). The catalog presented here is sufficiently detailed to map earthquakes to individual faults, but the published post-seismic slip models do not have sufficiently detailed crustal fault resolution to directly compare aftershocks with afterslip. Because of the complexity of the earthquake, GNSS displacement measured at a single site is likely to correspond to slip on multiple fault sources, rendering direct comparison of geodetic data with seismicity non-unique. Nevertheless, despite the range of faulting and co-seismic slip, it appears that aftershock distributions correlate well with geodetically determined displacements, suggesting that aftershocks are driven by local afterslip (Frank et al., 2017; Perfettini et al., 2018).

707

5 Conclusions

708

709

710

711

712

713

714

715

The 2016 M 7.8 Kaikōura earthquake is widely regarded as one of the most complex earthquakes in recorded history (Hamling, 2020). Detailed mapping of seismicity around the faults that ruptured in the Kaikōura earthquake further emphasises this complexity: at-least in the post-seismic period, multiple faults that did not have surface rupture are activated including two of the high slip-rate and high hazard Marlborough Faults (the Clarence and the Hope Faults). However, the additional faults observable through this mapping may also simplify some of the kinematics of the rupture by providing additional structures to host variations in slip between nearby fault segments.

716

717

To address the original outstanding questions outlined in Section 1.3, and as discussed in Sections 4.1–4.5, our conclusions are as follows:

718

719

720

1. The mainshock unequivocally nucleated on the Humps Fault. Previous scatter in published locations can be attributed to inappropriate location methods or data quality issues which we have thoroughly addressed in this study.

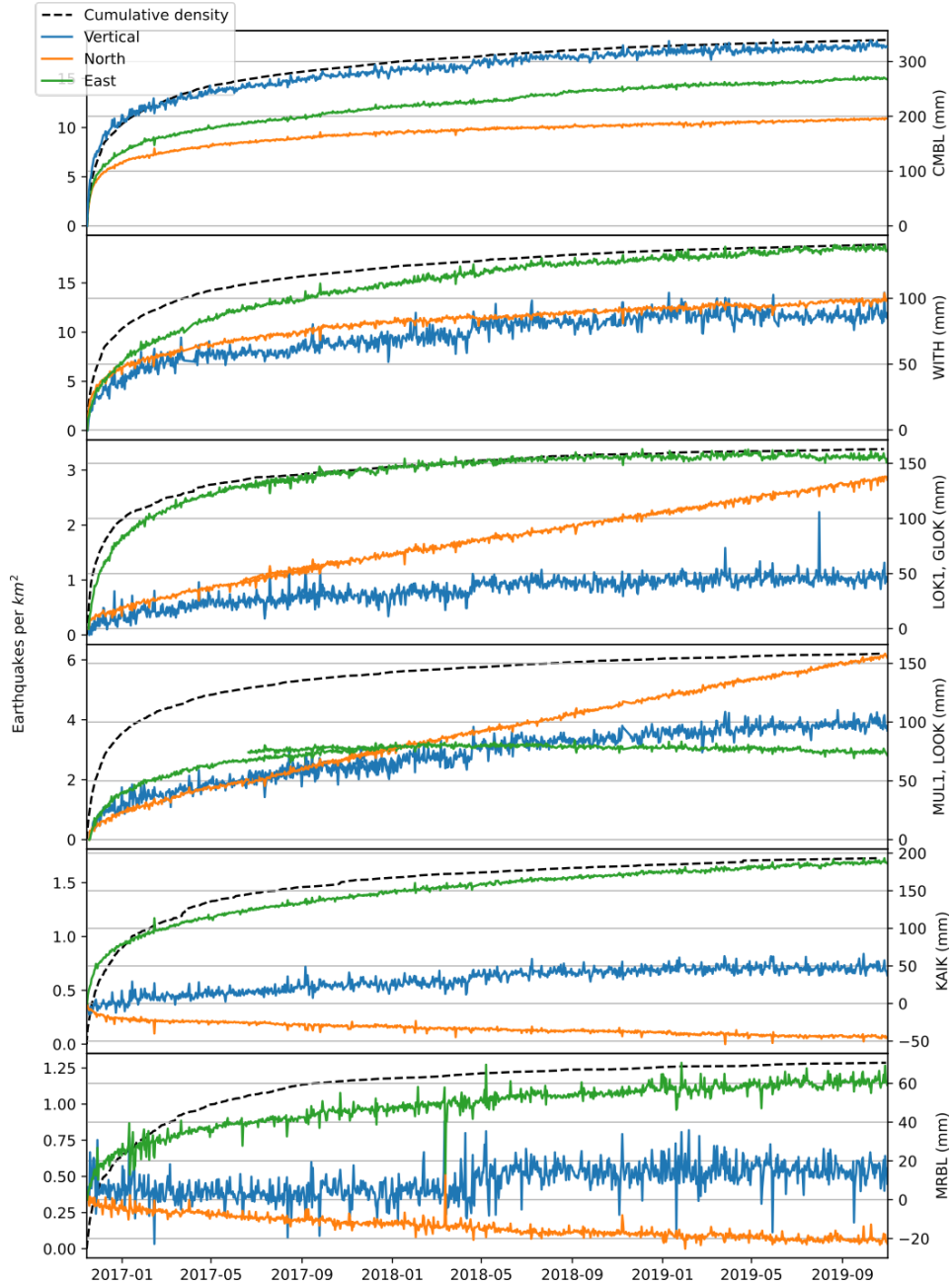


Figure 9. GPS time-series and cumulative aftershock density for regions around the Kaikōura afterslip region. Regions are ordered north (top) to south. GPS displacements for sites CMBL, WITH, KAIK and MRBL have a long-term gradient removed (calculated between 2015/01/01 to 2016/11/1). Sites LOK1, GLOK, MUL1 and LOOK have not had any gradient removed because they were not active prior to Kaikōura. Data from stations GLOK and LOOK have been shifted to have matching displacements at the end of the recording periods of LOK1 and MUL1 respectively. Note that the overlap is imperfect, but provides a representative view of displacement in the region. In general the evolution of the aftershock sequence matches the evolution of the displacement for these regions, however there are strong differences across the regions highlighting different amounts of afterslip.

- 721 2. Offshore thrust faulting illuminated by aftershocks suggests a physical connection
722 between the Hundalee and Papatea Faults, which may explain anomalously high
723 slip on the Papatea Fault and provides a likely southern/offshore rupture route.
- 724 3. The Snowgrass-Papatea-Jordan Thrust-Kekerengu system acts as a quadruple junc-
725 tion providing a means of distributing the drop in slip between the Kekerengu and
726 Jordan Thrust Faults.
- 727 4. Both the Hope and Clarence Faults were active post-seismically and produced af-
728 tershocks, though these were not laterally extensive, and occur near fault junc-
729 tions or transitional zones.
- 730 5. The rupture terminated near the epicentres of the Lake Grassmere and Cook Strait
731 2013 earthquakes, and likely re-ruptured these faults. The Cook Strait and Lake
732 Grassmere faults are more favourably oriented for slip than the co-seismically rup-
733 tured Needles Fault, and we propose that the combination of unfavourable orien-
734 tation of the Needles together with reduced pre-stress on the Lake Grassmere and
735 Cook Strait faults was sufficient to cause the rupture to terminate here.
- 736 6. We observe very few aftershocks on the subduction interface. A proportion of the
737 afterslip previously mapped onto the subduction interface may instead be accom-
738 modated by unmodelled upper crustal faults, such as the previously unidentified
739 Snowgrass Fault, the Clarence Fault and diffuse faulting characterised by abun-
740 dant aftershocks near Cape Campbell. However crustal faults are unlikely to re-
741 move the need for deep deformation to explain the long-wavelength signature in
742 the geodetic data, but this deformation likely occurs aseismically.

743 Considering all of the above, we infer that the Kaikōura earthquake nucleated with-
744 out significant detectable precursory seismicity on the Humps Fault before transition-
745 ing through the Leader/Stone Jug system and onto the Hundalee Fault. The rupture then
746 continued directly onto the offshore fault system characterised by reverse slip, elsewhere
747 called the Point Keen Fault. Slip then transitioned onto the Papatea Fault, likely by di-
748 rectly linked faults at depth in a thrust block bounded by sinistral faulting on the Pa-
749 patea and Snowgrass Faults (Figure 6). Within this block, the Jordan Thrust Fault was
750 reactivated in an extensional stress regime giving rise to normal motion (in contrast to
751 the long-term motion on this fault), and the difference in slip between the Jordan Thrust
752 and Kekerengu Faults is accommodated by buried slip on the previously unknown Snow-
753 grass Fault.

754 Slip then transitioned onto the Kekerengu Fault, which experienced near-total stress-
755 drop in the high slip patch identified by other authors (e.g. Kearse et al., 2018), and char-
756 acterised here by a lack of aftershocks. The rupture then propagated onto the Needles
757 Fault and other faults around Cape Campbell that were previously ruptured in the 2013
758 Cook Strait earthquakes. A combination of an unfavourable stress orientation on the Ne-
759 edles Fault and reduced pre-stress due to recent slip on the Cook Strait and Lake Grass-
760 mere faults resulted in the termination of the Kaikōura earthquake at Cape Campbell.
761 We see no evidence for seismic slip on an underlying subduction interface, apart from
762 a small cluster of interface related seismicity near Cape Campbell. We therefore suggest
763 that the boundary between the overriding Australian plate and subduction Pacific plate
764 may be ductile beneath much of the Kaikōura earthquake fault system as suggested by
765 Eberhart-Phillips et al. (2021).

766 Data Availability

767 All waveform data were downloaded from GeoNet via their FDSN client (last ac-
768 cessed 20 April 2021). The catalog generated here is available at <https://doi.org/10.5281/zenodo.4717333>
769 (last accessed 24 April 2021) in QUAKEML and CSV format.

770 **Acknowledgments**

771 Chamberlain and Townend are grateful to New Zealand’s Earthquake Commission
 772 (EQC) for funding through the EQC Programme in Seismology and Tectonic Geodesy
 773 at Victoria University of Wellington, and an EQC Biennial Grant (18/753), and to the
 774 Royal Society of New Zealand for funding through the Marsden Fast-Start project 17-
 775 VUW-121. Frank, Townend and Chamberlain also received funding for this collabora-
 776 tion through the New Zealand Royal Societies Catalyst Grant scheme. Chamberlain and
 777 Warren-Smith are grateful to the New Zealand Ministry of Business, Innovation and Em-
 778 ployment for funding through the Endeavour programme: ‘Rapid Characterisation of Earth-
 779 quakes and Tsunamis (RCET). Warren-Smith was funded through GNS Science Min-
 780 istry of Business Innovation and Employment strategic science investment funding (GNS-
 781 SSIF). Initial compute time was provided by the New Zealand eScience Infrastructure
 782 (NeSI) for which we are grateful. Later computations were run on Amazon Web Services,
 783 with data handling assistance from GeoNet. ObsPy (Krischer et al., 2015) was used ex-
 784 tensively throughout this work, figures were made using matplotlib (Hunter, 2007) and
 785 cartopy (Met Office, 2010 - 2015), and we are very grateful to the developers and main-
 786 tainers of these open-source projects who enable complex science. Finally we are grate-
 787 ful to Tim Little and Andy Howell for informative discussions during the preparation
 788 of this work.

789 **References**

- 790 Ando, R., & Kaneko, Y. (2018). Dynamic rupture simulation reproduces sponta-
 791 neous multifault rupture and arrest during the 2016 mw 7.9 kaikoura earth-
 792 quake. *Geophysical Research Letters*, *45*(23), 12,875–12,883. Retrieved
 793 from [https://agupubs.onlinelibrary.wiley.com/doi/abs/10.1029/](https://agupubs.onlinelibrary.wiley.com/doi/abs/10.1029/2018GL080550)
 794 [2018GL080550](https://agupubs.onlinelibrary.wiley.com/doi/abs/10.1029/2018GL080550) doi: 10.1029/2018GL080550
- 795 Bai, Y., Lay, T., Cheung, K. F., & Ye, L. (2017). Two regions of seafloor deforma-
 796 tion generated the tsunami for the 13 november 2016, kaikoura, new zealand
 797 earthquake. *Geophysical Research Letters*, *44*(13), 6597–6606. Retrieved
 798 from [https://agupubs.onlinelibrary.wiley.com/doi/abs/10.1002/](https://agupubs.onlinelibrary.wiley.com/doi/abs/10.1002/2017GL073717)
 799 [2017GL073717](https://agupubs.onlinelibrary.wiley.com/doi/abs/10.1002/2017GL073717) doi: 10.1002/2017GL073717
- 800 Balfour, N., Savage, M., & Townend, J. (2005). Stress and crustal anisotropy in
 801 marlborough, new zealand: evidence for low fault strength and structure-
 802 controlled anisotropy. *Geophysical Journal International*, *163*(3), 1073–1086.
- 803 Bradley, B. A., Razafindrakoto, H. N., & Polak, V. (2017). Ground-motion obser-
 804 vations from the 14 november 2016 m w 7.8 kaikoura, new zealand, earthquake
 805 and insights from broadband simulations. *Seismological Research Letters*,
 806 *88*(3), 740–756.
- 807 Bratt, S., & Nagy, W. (1991). The locsat program. *Science Applications Interna-*
 808 *tional Corporation, San Diego.*
- 809 Cesca, S., Zhang, Y., Mouslopoulou, V., Wang, R., Saul, J., Savage, M., ... Dahm,
 810 T. (2017). Complex rupture process of the mw 7.8, 2016, kaikoura earth-
 811 quake, new zealand, and its aftershock sequence. *Earth and Planetary Science*
 812 *Letters*, *478*, 110 - 120. Retrieved from [http://www.sciencedirect.com/](http://www.sciencedirect.com/science/article/pii/S0012821X17304715)
 813 [science/article/pii/S0012821X17304715](http://www.sciencedirect.com/science/article/pii/S0012821X17304715) doi: [https://doi.org/10.1016/](https://doi.org/10.1016/j.epsl.2017.08.024)
 814 [j.epsl.2017.08.024](https://doi.org/10.1016/j.epsl.2017.08.024)
- 815 Chamberlain, C. J., Hopp, C. J., Boese, C. M., Warren-Smith, E., Chambers, D.,
 816 Chu, S. X., ... Townend, J. (2018). Eqcorrscan: Repeating and near-repeating
 817 earthquake detection and analysis in python. *Seismological Research Letters*,
 818 *89*(1), 173–181.
- 819 Chamberlain, C. J., Townend, J., & Gerstenberger, M. C. (2020). Rt-eqcorrscan:
 820 Near-real-time matched-filtering for rapid development of dense earthquake
 821 catalogs. *Seismological Society of America*, *91*(6), 3574–3584.

- 822 Christophersen, A., Rhoades, D., Gerstenberger, M., Bannister, S., Becker, J., Pot-
 823 ter, S., & McBride, S. (2017). Progress and challenges in operational earth-
 824 quake forecasting in new zealand. In *New zealand society for earthquake*
 825 *engineering annual technical conference*.
- 826 Clark, K., Nissen, E., Howarth, J., Hamling, I., Mountjoy, J., Ries, W., ... Strong,
 827 D. (2017). Highly variable coastal deformation in the 2016 mw7.8 kaikōura
 828 earthquake reflects rupture complexity along a transpressional plate bound-
 829 ary. *Earth and Planetary Science Letters*, *474*, 334 - 344. Retrieved from
 830 <http://www.sciencedirect.com/science/article/pii/S0012821X17303722>
 831 doi: <https://doi.org/10.1016/j.epsl.2017.06.048>
- 832 Darby, D. J., & Beanland, S. (1992). Possible source models for the 1855 wairarapa
 833 earthquake, new zealand. *Journal of Geophysical Research: Solid Earth*,
 834 *97*(B9), 12375–12389.
- 835 Diederichs, A., Nissen, E., Lajoie, L., Langridge, R., Malireddi, S., Clark, K., ...
 836 Tagliasacchi, A. (2019). Unusual kinematics of the papatea fault (2016
 837 kaikōura earthquake) suggest anelastic rupture. *Science advances*, *5*(10),
 838 eaax5703.
- 839 Eberhart-Phillips, D., & Bannister, S. (2015). 3-d imaging of the northern hikurangi
 840 subduction zone, new zealand: variations in subducted sediment, slab fluids
 841 and slow slip. *Geophysical Journal International*, *201*(2), 838–855.
- 842 Eberhart-Phillips, D., Bannister, S., & Reyners, M. (2017, November). *New*
 843 *Zealand Wide model 2.1 seismic velocity model for New Zealand*. Zen-
 844 odo. Retrieved from <https://doi.org/10.5281/zenodo.1043558> doi:
 845 10.5281/zenodo.1043558
- 846 Eberhart-Phillips, D., Ellis, S., Lanza, F., & Bannister, S. (2021). Heterogeneous
 847 material properties – as inferred from seismic attenuation - influenced multi-
 848 ple fault rupture and ductile creep of the Kaikoura Mw 7.8 earthquake, New
 849 Zealand. *Geophysical Journal International*.
- 850 Frank, W. B., Poli, P., & Perfettini, H. (2017). Mapping the rheology of the central
 851 chile subduction zone with aftershocks. *Geophysical Research Letters*, *44*(11),
 852 5374–5382.
- 853 Frigo, M., & Johnson, S. G. (1998). Fftw: An adaptive software architecture for
 854 the fft. In *Proceedings of the 1998 ieee international conference on acous-*
 855 *tics, speech and signal processing, icassp'98 (cat. no. 98ch36181)* (Vol. 3, pp.
 856 1381–1384).
- 857 Gusman, A. R., Satake, K., Gunawan, E., Hamling, I., & Power, W. (2018). Con-
 858 tribution from multiple fault ruptures to tsunami generation during the 2016
 859 kaikoura earthquake. *Pure and Applied Geophysics*, *175*(8), 2557–2574.
- 860 Hainzl, S. (2016). Rate-dependent incompleteness of earthquake catalogs. *Seismolog-*
 861 *ical Research Letters*, *87*(2A), 337–344.
- 862 Hamling, I. J. (2020). A review of the 2016 kaikōura earthquake: insights from
 863 the first 3 years. *Journal of the Royal Society of New Zealand*, *50*(2), 226-244.
 864 Retrieved from <https://doi.org/10.1080/03036758.2019.1701048> doi: 10
 865 .1080/03036758.2019.1701048
- 866 Hamling, I. J., D'Anastasio, E., Wallace, L. M., Ellis, S., Motagh, M., Samsonov, S.,
 867 ... Hreinsdóttir, S. (2014). Crustal deformation and stress transfer during
 868 a propagating earthquake sequence: The 2013 cook strait sequence, central
 869 new zealand. *Journal of Geophysical Research: Solid Earth*, *119*(7), 6080-
 870 6092. Retrieved from [https://agupubs.onlinelibrary.wiley.com/doi/abs/](https://agupubs.onlinelibrary.wiley.com/doi/abs/10.1002/2014JB011084)
 871 [10.1002/2014JB011084](https://doi.org/10.1002/2014JB011084) doi: 10.1002/2014JB011084
- 872 Hamling, I. J., Hreinsdóttir, S., Clark, K., Elliott, J., Liang, C., Fielding, E., ...
 873 Stirling, M. (2017). Complex multifault rupture during the 2016 mw 7.8
 874 kaikoura earthquake, new zealand. *Science*, *356*(6334). Retrieved from
 875 <https://science.sciencemag.org/content/356/6334/eaam7194> doi:
 876 10.1126/science.aam7194

- 877 Harris, R. A., Archuleta, R. J., & Day, S. M. (1991). Fault steps and the dynamic
878 rupture process: 2-d numerical simulations of a spontaneously propagating
879 shear fracture. *Geophysical Research Letters*, *18*(5), 893–896.
- 880 Henrys, S., Eberhart-Phillips, D., Bassett, D., Sutherland, R., Okaya, D., Savage,
881 M., ... others (2020). Upper plate heterogeneity along the southern hikurangi
882 margin, new zealand. *Geophysical Research Letters*, *47*(4), e2019GL085511.
- 883 Holden, C., Kaneko, Y., D’Anastasio, E., Benites, R., Fry, B., & Hamling, I. J.
884 (2017). The 2016 kaikōura earthquake revealed by kinematic source inversion
885 and seismic wavefield simulations: Slow rupture propagation on a geometrically
886 complex crustal fault network. *Geophysical Research Letters*, *44*(22), 11,320-
887 11,328. Retrieved from [https://agupubs.onlinelibrary.wiley.com/doi/
888 abs/10.1002/2017GL075301](https://agupubs.onlinelibrary.wiley.com/doi/abs/10.1002/2017GL075301) doi: 10.1002/2017GL075301
- 889 Howell, A., Nissen, E., Stahl, T., Clark, K., Kears, J., Van Dissen, R., ... Jones,
890 K. (2020). Three-dimensional surface displacements during the 2016 mw
891 7.8 kaikōura earthquake (new zealand) from photogrammetry-derived point
892 clouds. *Journal of Geophysical Research: Solid Earth*, *125*(1), e2019JB018739.
893 Retrieved from [https://agupubs.onlinelibrary.wiley.com/doi/abs/
894 10.1029/2019JB018739](https://agupubs.onlinelibrary.wiley.com/doi/abs/10.1029/2019JB018739) (e2019JB018739 2019JB018739) doi: 10.1029/
895 2019JB018739
- 896 Hunter, J. D. (2007). Matplotlib: A 2d graphics environment. *Computing in Science
897 & Engineering*, *9*(3), 90–95. doi: 10.1109/MCSE.2007.55
- 898 Kaiser, A., Balfour, N., Fry, B., Holden, C., Litchfield, N., Gerstenberger, M., ...
899 Gledhill, K. (2017, 04). The 2016 Kaikōura, New Zealand, Earthquake:
900 Preliminary Seismological Report. *Seismological Research Letters*, *88*(3),
901 727–739. Retrieved from <https://doi.org/10.1785/0220170018> doi:
902 10.1785/0220170018
- 903 Kears, J., Little, T. A., Van Dissen, R. J., Barnes, P. M., Langridge, R., Moun-
904 tjoy, J., ... Hemphill-Haley, M. (2018, 04). Onshore to Offshore Ground-
905 Surface and Seabed Rupture of the Jordan–Kekerengu–Needles Fault Network
906 during the 2016 Mw 7.8 Kaikōura Earthquake, New Zealand. *Bulletin of
907 the Seismological Society of America*, *108*(3B), 1573–1595. Retrieved from
908 <https://doi.org/10.1785/0120170304> doi: 10.1785/0120170304
- 909 Kennett, B., & Engdahl, E. (1991). Traveltimes for global earthquake location and
910 phase identification. *Geophysical Journal International*, *105*(2), 429–465.
- 911 King, G. C., Stein, R. S., & Lin, J. (1994). Static stress changes and the triggering
912 of earthquakes. *Bulletin of the Seismological Society of America*, *84*(3), 935–
913 953.
- 914 Klinger, Y., Okubo, K., Vallage, A., Champenois, J., Delorme, A., Rougier, E., ...
915 others (2018). Earthquake damage patterns resolve complex rupture processes.
916 *Geophysical Research Letters*, *45*(19), 10–279.
- 917 Krischer, L., Megies, T., Barsch, R., Beyreuther, M., Lecocq, T., Caudron, C., &
918 Wassermann, J. (2015). Obspy: A bridge for seismology into the scientific
919 python ecosystem. *Computational Science & Discovery*, *8*(1), 014003.
- 920 Lamb, S., Arnold, R., & Moore, J. D. (2018). Locking on a megathrust as a cause
921 of distributed faulting and fault-jumping earthquakes. *Nature Geoscience*,
922 *11*(11), 871–875.
- 923 Langridge, R., Ries, W., Litchfield, N., Villamor, P., Van Dissen, R., Barrell, D., ...
924 others (2016). The new zealand active faults database. *New Zealand Journal
925 of Geology and Geophysics*, *59*(1), 86–96.
- 926 Langridge, R. M., Rowland, J., Villamor, P., Mountjoy, J., Townsend, D. B., Nis-
927 sen, E., ... Hamling, I. (2018, 06). Coseismic Rupture and Preliminary Slip
928 Estimates for the Papatea Fault and Its Role in the 2016 Mw 7.8 Kaikōura,
929 New Zealand, Earthquake. *Bulletin of the Seismological Society of America*,
930 *108*(3B), 1596–1622. Retrieved from <https://doi.org/10.1785/0120170336>
931 doi: 10.1785/0120170336

- 932 Lanza, F., Chamberlain, C. J., Jacobs, K., Warren-Smith, E., Godfrey, H. J., Ko-
 933 rtink, M., ... Eberhart-Phillips, D. (2019). Crustal fault connectivity of
 934 the mw 7.8 2016 kaikōura earthquake constrained by aftershock relocations.
 935 *Geophysical Research Letters*, *46*(12), 6487-6496. Retrieved from [https://](https://agupubs.onlinelibrary.wiley.com/doi/abs/10.1029/2019GL082780)
 936 agupubs.onlinelibrary.wiley.com/doi/abs/10.1029/2019GL082780 doi:
 937 10.1029/2019GL082780
- 938 Lienert, B. R., & Havskov, J. (1995). A computer program for locating earthquakes
 939 both locally and globally. *Seismological Research Letters*, *66*(5), 26–36.
- 940 Litchfield, N. J., Villamor, P., Dissen, R. J. V., Nicol, A., Barnes, P. M., A. Bar-
 941 rell, D. J., ... others (2018). Surface rupture of multiple crustal faults in the
 942 2016 m w 7.8 kaikōura, new zealand, earthquake. *Bulletin of the Seismological*
 943 *Society of America*, *108*(3B), 1496–1520.
- 944 Lomax, A., Virieux, J., Volant, P., & Berge-Thierry, C. (2000). Probabilistic earth-
 945 quake location in 3d and layered models. In *Advances in seismic event location*
 946 (pp. 101–134). Springer.
- 947 Met Office. (2010 - 2015). Cartopy: a cartographic python library with a mat-
 948 plotlib interface [Computer software manual]. Exeter, Devon. Retrieved from
 949 <https://scitools.org.uk/cartopy>
- 950 Michailos, K., Smith, E. G., Chamberlain, C. J., Savage, M. K., & Townend, J.
 951 (2019). Variations in seismogenic thickness along the central alpine fault,
 952 new zealand, revealed by a decade’s relocated microseismicity. *Geochemistry,*
 953 *Geophysics, Geosystems*, *20*(1), 470–486.
- 954 Mouslopoulou, V., Saltogianni, V., Nicol, A., Oncken, O., Begg, J., Babeyko,
 955 A., ... Moreno, M. (2019). Breaking a subduction-termination from
 956 top to bottom: The large 2016 kaikōura earthquake, new zealand. *Earth*
 957 *and Planetary Science Letters*, *506*, 221 - 230. Retrieved from [http://](http://www.sciencedirect.com/science/article/pii/S0012821X18306162)
 958 www.sciencedirect.com/science/article/pii/S0012821X18306162 doi:
 959 <https://doi.org/10.1016/j.epsl.2018.10.020>
- 960 Nicol, A., Khajavi, N., Pettinga, J. R., Fenton, C., Stahl, T., Bannister, S., ... Mc-
 961 Coll, S. T. (2018, 05). Preliminary Geometry, Displacement, and Kinematics
 962 of Fault Ruptures in the Epicentral Region of the 2016 Mw 7.8 Kaikōura,
 963 New Zealand, Earthquake. *Bulletin of the Seismological Society of America*,
 964 *108*(3B), 1521-1539. Retrieved from <https://doi.org/10.1785/0120170329>
 965 doi: 10.1785/0120170329
- 966 Okada, T., Iio, Y., Matsumoto, S., Bannister, S., Ohmi, S., Horiuchi, S., ... others
 967 (2019). Comparative tomography of reverse-slip and strike-slip seismotectonic
 968 provinces in the northern south island, new zealand. *Tectonophysics*, *765*,
 969 172–186.
- 970 Peng, Z., Fry, B., Chao, K., Yao, D., Meng, X., & Jolly, A. (2018, 05). Remote
 971 Triggering of Microearthquakes and Tremor in New Zealand following the
 972 2016 Mw 7.8 Kaikōura Earthquake. *Bulletin of the Seismological Society of*
 973 *America*, *108*(3B), 1784-1793. Retrieved from [https://doi.org/10.1785/](https://doi.org/10.1785/0120170327)
 974 [0120170327](https://doi.org/10.1785/0120170327) doi: 10.1785/0120170327
- 975 Perfettini, H., Frank, W., Marsan, D., & Bouchon, M. (2018). A model of aftershock
 976 migration driven by afterslip. *Geophysical Research Letters*, *45*(5), 2283–2293.
- 977 Plesch, A., Shaw, J. H., Ross, Z. E., & Hauksson, E. (2020). Detailed 3d fault repre-
 978 sentations for the 2019 ridgecrest, california, earthquake sequence. *Bulletin of*
 979 *the Seismological Society of America*, *110*(4), 1818–1831.
- 980 Rattenbury, M., & Isaac, M. (2012). The qmap 1: 250 000 geological map of new
 981 zealand project. *New Zealand Journal of Geology and Geophysics*, *55*(4), 393–
 982 405.
- 983 Ristau, J. (2013). Update of regional moment tensor analysis for earthquakes in new
 984 zealand and adjacent offshore regions. *Bulletin of the Seismological Society of*
 985 *America*, *103*(4), 2520–2533.
- 986 Rodgers, D., & Little, T. (2006). World’s largest coseismic strike-slip offset: The

- 1855 rupture of the wairarapa fault, new zealand, and implications for displacement/length scaling of continental earthquakes. *Journal of Geophysical Research: Solid Earth*, *111*(B12).
- Romanet, P., & Ide, S. (2019). Ambient tectonic tremors in manawatu, cape tur-nagain, marlborough, and puysegur, new zealand. *Earth, Planets and Space*, *71*(1), 1–9.
- Senobari, N. S., Funning, G. J., Keogh, E., Zhu, Y., Yeh, C.-C. M., Zimmerman, Z., & Mueen, A. (2019). Super-efficient cross-correlation (sec-c): A fast matched filtering code suitable for desktop computers. *Seismological Research Letters*, *90*(1), 322–334.
- Stirling, M., McVerry, G., Gerstenberger, M., Litchfield, N., Van Dissen, R., Berryman, K., ... others (2012). National seismic hazard model for new zealand: 2010 update. *Bulletin of the Seismological Society of America*, *102*(4), 1514–1542.
- Tan, F., Ge, Z., Kao, H., & Nissen, E. (2019). Validation of the 3-d phase-weighted relative back projection technique and its application to the 2016 m w 7.8 kaikōura earthquake. *Geophysical Journal International*, *217*(1), 375–388.
- Townend, J., Sherburn, S., Arnold, R., Boese, C., & Woods, L. (2012). Three-dimensional variations in present-day tectonic stress along the australia–pacific plate boundary in new zealand. *Earth and Planetary Science Letters*, *353*, 47–59.
- Trugman, D. T., & Shearer, P. M. (2017). Growclust: A hierarchical clustering algorithm for relative earthquake relocation, with application to the spanish springs and sheldon, nevada, earthquake sequences. *Seismological Research Letters*, *88*(2A), 379–391.
- Ulrich, T., Gabriel, A.-A., Ampuero, J.-P., & Xu, W. (2019). Dynamic viability of the 2016 mw 7.8 kaikōura earthquake cascade on weak crustal faults. *Nature Communications*. doi: 10.1038/s41467-019-09125
- Van Dissen, R., & Nicol, A. (2009). Mid-late holocene paleoseismicity of the eastern clarence fault, marlborough, new zealand. *New Zealand Journal of Geology and Geophysics*, *52*(3), 195–208.
- Van Dissen, R., & Yeats, R. S. (1991). Hope fault, jordan thrust, and uplift of the seaward kaikoura range, new zealand. *Geology*, *19*(4), 393–396.
- Waldhauser, F., & Ellsworth, W. L. (2000). A double-difference earthquake location algorithm: Method and application to the northern hayward fault, california. *Bulletin of the Seismological Society of America*, *90*(6), 1353–1368.
- Wallace, L. M., Hreinsdóttir, S., Ellis, S., Hamling, I., D’Anastasio, E., & Denys, P. (2018). Triggered slow slip and afterslip on the southern hikurangi subduction zone following the kaikōura earthquake. *Geophysical Research Letters*, *45*(10), 4710–4718. Retrieved from <https://agupubs.onlinelibrary.wiley.com/doi/abs/10.1002/2018GL077385> doi: 10.1002/2018GL077385
- Wallace, L. M., Kaneko, Y., Hreinsdóttir, S., Hamling, I., Peng, Z., Bartlow, N., ... Fry, B. (2017). Large-scale dynamic triggering of shallow slow slip enhanced by overlying sedimentary wedge. *Nature Geoscience*. doi: 10.1038/NGEO3021
- Walsh, D., Arnold, R., & Townend, J. (2009). A bayesian approach to determining and parametrizing earthquake focal mechanisms. *Geophysical Journal International*, *176*(1), 235–255.
- Wang, D., Chen, Y., Wang, Q., & Mori, J. (2018). Complex rupture of the 13 november 2016 mw 7.8 kaikoura, new zealand earthquake: Comparison of high-frequency and low-frequency observations. *Tectonophysics*, *733*, 100–107. Retrieved from <https://www.sciencedirect.com/science/article/pii/S0040195118300647> (Physics of Earthquake Rupture Propagation) doi: <https://doi.org/10.1016/j.tecto.2018.02.004>
- Wang, T., Jiao, L., Tapponnier, P., Shi, X., & Wei, S. (2020). Space imaging geodesy reveals near circular, coseismic block rotation during the 2016 mw

- 1042 7.8 kaikōura earthquake, new zealand. *Geophysical Research Letters*, 47(22),
 1043 e2020GL090206.
- 1044 Wang, T., Wei, S., Shi, X., Qiu, Q., Li, L., Peng, D., . . . Barbot, S. (2018). The
 1045 2016 kaikōura earthquake: Simultaneous rupture of the subduction interface
 1046 and overlying faults. *Earth and Planetary Science Letters*, 482, 44–51.
- 1047 Warren-Smith, E., Chamberlain, C. J., Lamb, S., & Townend, J. (2017). High-
 1048 precision analysis of an aftershock sequence using matched-filter detection:
 1049 The 4 may 2015 ml 6 wanaka earthquake, southern alps, new zealand. *Seismo-*
 1050 *logical Research Letters*, 88(4), 1065–1077.
- 1051 Wesnousky, S. G. (2006). Predicting the endpoints of earthquake ruptures. *Nature*,
 1052 444(7117), 358–360.
- 1053 Wiemer, Stefan and Wyss, Max. (2000). Minimum magnitude of completeness in
 1054 earthquake catalogs: Examples from Alaska, the western United States, and
 1055 Japan. *Bulletin of the Seismological Society of America*, 90(4), 859–869.
- 1056 Williams, C. A., Eberhart-Phillips, D., Bannister, S., Barker, D. H. N., Henrys, S.,
 1057 Reyners, M., & Sutherland, R. (2013). Revised interface geometry for the
 1058 hikurangi subduction zone, new zealand. *Seismological Research Letters*, 84(6),
 1059 1066–1073.
- 1060 Williams, J. N., Barrell, D. J. A., Stirling, M. W., Sauer, K. M., Duke, G. C., &
 1061 Hao, K. X. (2018, 06). Surface Rupture of the Hundalee Fault during the
 1062 2016 Mw 7.8 Kaikōura Earthquake. *Bulletin of the Seismological Society of*
 1063 *America*, 108(3B), 1540-1555. Retrieved from [https://doi.org/10.1785/](https://doi.org/10.1785/0120170291)
 1064 [0120170291](https://doi.org/10.1785/0120170291) doi: 10.1785/0120170291
- 1065 Xu, W., Feng, G., Meng, L., Zhang, A., Ampuero, J. P., Bürgmann, R., & Fang, L.
 1066 (2018). Transpressional rupture cascade of the 2016 mw 7.8 kaikoura earth-
 1067 quake, new zealand. *Journal of Geophysical Research: Solid Earth*, 123(3),
 1068 2396-2409. Retrieved from [https://agupubs.onlinelibrary.wiley.com/](https://agupubs.onlinelibrary.wiley.com/doi/abs/10.1002/2017JB015168)
 1069 doi/abs/10.1002/2017JB015168 doi: 10.1002/2017JB015168
- 1070 Yao, D., Peng, Z., Kaneko, Y., Fry, B., & Meng, X. (2021). Dynamic triggering
 1071 of earthquakes in the north island of new zealand following the 2016 mw 7.8
 1072 kaikōura earthquake. *Earth and Planetary Science Letters*, 557, 116723.
- 1073 Yu, C., Li, Z., & Penna, N. T. (2020). Triggered afterslip on the southern Hikurangi
 1074 subduction interface following the 2016 Kaikōura earthquake from InSAR time
 1075 series with atmospheric corrections. *Remote Sensing of Environment*, 251,
 1076 112097.
- 1077 Zinke, R., Hollingsworth, J., Dolan, J. F., & Van Dissen, R. (2019). Three-
 1078 dimensional surface deformation in the 2016 mw 7.8 kaikōura, new zealand,
 1079 earthquake from optical image correlation: Implications for strain localization
 1080 and long-term evolution of the pacific-australian plate boundary. *Geochem-*
 1081 *istry, Geophysics, Geosystems*, 20(3), 1609–1628.